Tectonics

RESEARCH ARTICLE
10.1029/2017TC004776

Key Points:
- A preexisting fault is reactivated in three modes: full, partial, or none, due to its strike angle to the extension direction
- A reactivated preexisting fault influences the density, orientation, length, and displacement of adjacent newly formed faults
- Fault interaction styles vary with respect to the reactivation mode of preexisting faults

How Does the Orientation of a Preexisting Basement Weakness Influence Fault Development During Renewed Rifting? Insights From Three-Dimensional Discrete Element Modeling

Chao Deng[1,2], Robert L. Gawthorpe[1], Haakon Fossen[3,1], and Emma Finch[4]

[1]Department of Earth Science, University of Bergen, Bergen, Norway, [2]Now at Department of Geology, Northwest University, Xi'an, China, [3]Museum of Natural History, University of Bergen, Bergen, Norway, [4]School of Earth and Environmental Sciences, University of Manchester, Manchester, UK

Correspondence to:
C. Deng,
dengchao0926@gmail.com

Citation:
Deng, C., Gawthorpe, R. L., Fossen, H., & Finch, E. (2018). How does the orientation of a preexisting basement weakness influence fault development during renewed rifting? Insights from three-dimensional discrete element modeling. *Tectonics*, *37*, 2221–2242. https://doi.org/10.1029/2017TC004776

Received 8 NOV 2017
Accepted 9 MAY 2018
Accepted article online 21 MAY 2018
Published online 27 JUL 2018

Abstract The variety in fault geometry, fault interaction style, and evolution of the fault network above a weak planar preexisting fault as a result of a change in the strike angle (α) of the preexisting fault relative to the extension direction is investigated using three-dimensional discrete element modeling. The preexisting fault shows three reactivation modes: (i) full reactivation ($\alpha \geq 60°$), (ii) partial reactivation ($\alpha = 45°$), and (iii) little or no reactivation ($\alpha = 30°$). A fully reactivated fault decreases the density, affects the orientation, and enhances the length and displacement of adjacent new faults. A partially reactivated fault generates some isolated fault segments along strike and also influences fault orientation. However, when the preexisting fault is not reactivated, its presence has little effect on the growth of new faults. Our study confirms that the reactivation pattern of a preexisting fault and its influence on new fault growth varies with its strike angle relative to the extension direction. It also demonstrates how a preexisting fault influences adjacent fault geometry and the fault network by changing the density, orientation, length, and displacement of newly formed faults. The work impacts understanding three-dimensional fault geometries, the distribution, and evolution of fault networks in rift basins affected by preexisting faults and on predicting the extension direction of renewed rifting.

1. Introduction

The reactivation of preexisting faults or structures and their effect on the development of newly formed normal faults has been noticed in a number of rift basins, such as the NW Shelf of Australia (e.g., Frankowicz & Mcclay, 2010), Gulf of Thailand (e.g., Morley et al., 2007, 2004), Gulf of Aden (e.g., Bellahsen et al., 2006; Lepvrier et al., 2002), Northern North Sea (e.g., Badley et al., 1988; Deng, Fossen, et al., 2017; Duffy et al., 2015; Færseth, 1996; Færseth et al., 1997; Fazlikhani et al., 2017; Odinsen et al., 2000; Whipp et al., 2014), East African Rift (Corti, 2009; Le Turdu et al., 1999; Lezzar et al., 2002; Muirhead & Kattenhorn, 2017), and Milne Point, Alaska (e.g., Nixon et al., 2014). Some studies have shown that reactivated preexisting faults interacted with, and intersected, newly formed faults during a subsequent phase of extension, creating noncollinear fault geometries (e.g., Deng, Fossen, et al., 2017; Duffy et al., 2015; Nixon et al., 2014). In contrast, other studies have observed that preexisting faults or structures remained inactive and were offset by newly formed faults during a later rift phase (e.g., Claringbould et al., 2017; Færseth et al., 1997; Færseth & Ravnås, 1998; Fazlikhani et al., 2017; Phillips et al., 2016; Tomasso et al., 2008). A question raised by these observations is to what extent reactivation during secondary rifting is controlled by the strike orientation of the preexisting fault relative to the new extension direction.

Previous studies indicate that the reactivation of preexisting faults depends on their relative strength with respect to the host rock (e.g., Bellahsen & Daniel, 2005; Dubois et al., 2002; Etheridge, 1986; Ranalli & Yin, 1990). Some studies also suggest that the orientation of preexisting faults relative to the extension direction significantly influences the likelihood of reactivation during a secondary extension phase (e.g., Bonini et al., 1997; Fazlikhani et al., 2017; Henza et al., 2010, 2011; Keep & McClay, 1997; Phillips et al., 2016). Furthermore, the minimum dip of reactivated preexisting faults is controlled by the internal friction coefficient of rocks (e.g., Huyghe & Mugnier, 1992; Krantz, 1991; Sibson, 1985). Questions remain, however,

about the influence of the strike orientation of a preexisting fault on its reactivation potential and on the evolution of a nearby fault network in three dimensions. For instance, how does a preexisting fault reactivate and grow in three dimensions during a later extension phase? How variable is the reactivation pattern of a preexisting fault with changing strikes, and what is its effect on the spatial and temporal evolution of adjacent faults during extension?

In this work we use numerical methods to investigate the three-dimensional geometry and evolution of a weak planar preexisting fault and its influence on the nearby fault network during extension, based on a few chosen orientations of the preexisting fault relative to the extension direction. A related recent study uses discrete element modeling (DEM) to investigate fault geometry and evolution in three dimensions during extension (Finch & Gawthorpe, 2017). The aim of this study is to better understand the influence of the orientation of a weak planar preexisting fault on the nearby fault network in three dimensions. The results provide insights into three-dimensional fault geometries, the distribution and evolution of fault networks in rift basins affected by preexisting faults, and some generic examples for interpreting fault growth history, fault interaction styles, and associated extension directions in rifts.

2. Methodology

2.1. Discrete Element Model

DEM was first used to study rock failure and soil mechanism (e.g., Bardet & Proubet, 1992; Cundall, 1971; Cundall & Strack, 1979; Kuhn, 1999; Mora & Place, 1993). Further improvement was successfully applied to investigate the development of structural features, such as the growth of normal faults (e.g., Egholm et al., 2007; Finch & Gawthorpe, 2017; Hardy, 2013; Hardy & Finch, 2006, 2007; Imber et al., 2004; Schöpfer et al., 2006, 2007a, 2007b), folding (Finch et al., 2003, 2004; Hardy & Finch, 2005), boudinage (Komoróczi et al., 2013), and contractional wedges in mechanical stratigraphy (Wenk & Huhn, 2013). In this discrete element model, the crust is treated as an assembly of spherical elements that interact in pairs through bonds (e.g., Cundall & Strack, 1979; Mora & Place, 1993, 1994; Figures 1a and 1b). In the upper crust, a bond between neighboring elements (element *i* and neighbor *j*) deforms in a brittle manner (Mora & Place, 1993; Figure 1b). The elastic force in a bond follows

$$F_{ijU} = \begin{cases} K(r - r_0), r < r_b, \text{intact bond} \\ K(r - r_0), r < r_0, \text{broken bond} \\ 0, \qquad r \geq r_0, \text{broken bond} \end{cases} \tag{1}$$

K is the bond stiffness (elastic constant), r_0 is the equilibrium separation, r_b is the breaking separation, and r is the current separation between element pairs. An attractive force is exerted on neighboring elements through an intact bond; that is, $r < r_b$ and is removed if a bond is broken; that is, $r > r_b$. Once broken, a bond is not allowed to heal, leaving neighboring elements to interact only through a repulsive force when they return to a compressive contact; that is, $r < r_0$.

In the lower crust, elements deform in a ductile way and interact through linear firmoviscous (Newtonian fluid) forces, representing a firmoviscous body (Ranalli, 1995). The forces consist of two components in parallel: an elastic force and a viscous force (Figure 1b). The component of the elastic force exists only when neighboring elements are in a compressive contact; that is, $r < r_0$, similar to the upper crust, being

$$F_{ijL}^{\text{elastic}} = \begin{cases} K_c(r - r_0), r < r_0 \\ 0, \qquad r > r_0 \end{cases} \tag{2}$$

K_c is the bond stiffness. The component of viscous force is

$$F_{ijL}^{\text{viscous}} = \eta \Delta \dot{x}_{ij} \tag{3}$$

Here η is the Kelvin viscosity and determined through empirical tests and $\Delta \dot{x}_{ij}$ is the relative velocity between element *i* and neighbor *j*. Due to the viscous nature of the material, elements in the lower crust may flow out of the model boundaries under gravitational loading. Thus, a repulsive force is implemented by introducing vertical boundary walls in the x and y component directions, which prevents elements exceeding the

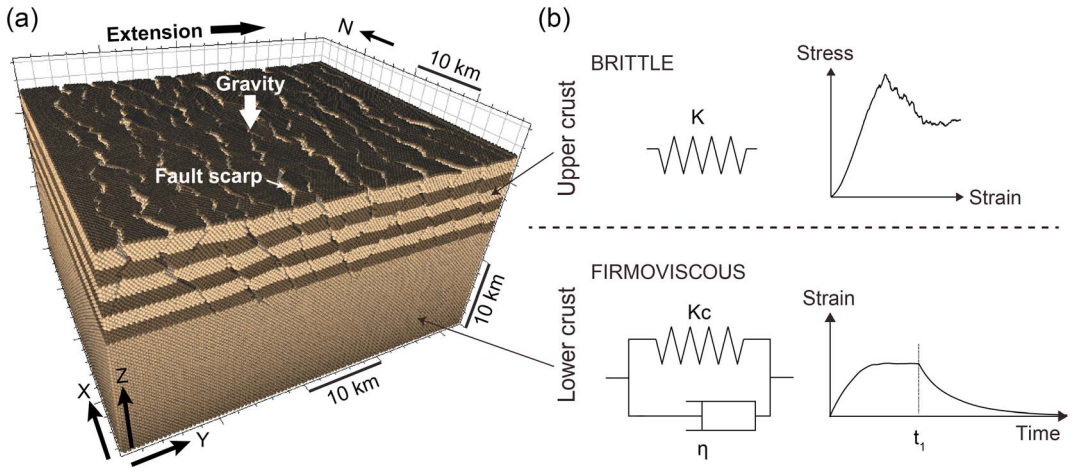

Figure 1. Discrete element modeling. (a) A modeling example of normal faults developing in extensional setting. The multilayers represent the upper crust, and the 15-km-thick bottom layer represents the lower crust. (b) Sketch of the forces within the upper and lower crust and their rheological response. In the upper crust, a bond breaks when stress reaches the breaking threshold. In the lower crust, strain increases with time under a load and decreases slowly when the load is removed at time t_1.

boundary. This simulates that the model exists within a larger system of elements with similar interaction properties. The force due to the boundary walls, F_{iB}, is given by

$$F_{iB} = -K_B r_B \tag{4}$$

K_B is the elastic stiffness of boundary walls and r_B is the distance by which an element exceeds the boundary (Wenk & Huhn, 2013).

To include a flexural response to loading through gravity, the elastic-brittle-plastic crust floats hydrostatically on a fluid mantle at a specific depth that depends on relative ratios of mantle and crust densities, which maintains the model in a hydrostatic equilibrium (King et al., 1988). Therefore, all elements experience an additional force, F_{iG}, due to gravity and flotation in the vertical, z component direction, which follows,

$$F_{iG} = g[(\rho_m - \rho_c)V_B - \rho_c V_A] \tag{5}$$

Here g is the gravitational acceleration, ρ_m is the mantle density, ρ_c is the crust density, and V_A and V_B are the volume of an element above and below the hydrostatic equilibrium, respectively.

As a model runs, kinetic energy will build up within the closed system because of dynamic phenomena such as reflected waves from the boundaries of the model (Donzé et al., 1994; Mora & Place, 1994, 1998). To keep the system less dynamic and more quasi-static, a damping force, F_{iD}, is applied, allowing energy to be dissipated (Donzé et al., 1994; Mora & Place, 1994, 1998). The damping force is

$$F_{iD} = v\Delta\dot{x}_{ij} \tag{6}$$

Here v is the dynamic viscosity, and $\Delta\dot{x}_{ij}$ is the relative velocity between elements. The value of the dynamic viscosity should be sufficiently small so that it will not modify the fundamental dynamics along faults and also be large enough to attenuate boundary reflections (Mora & Place, 1994).

Shear forces between elements are not considered in the model. Nevertheless, previous DEM studies have proven that realistic crustal deformation, such as the frictional stick-slip instability and normal faulting in mechanical stratigraphy can be successfully simulated in frictionless rock mass (e.g., Donzé et al., 1994; Finch et al., 2003, 2004; Hardy & Finch, 2007; Mora & Place, 1994, 1998). In addition, no consideration of friction reduces computation time. Therefore, the total force exerted on an element, i, in the upper crust is

$$F_{iU}^{\text{Total}} = \sum_{j=1,n} F_{ijU} + F_{iB} + F_{iG} + F_{iD} \tag{7}$$

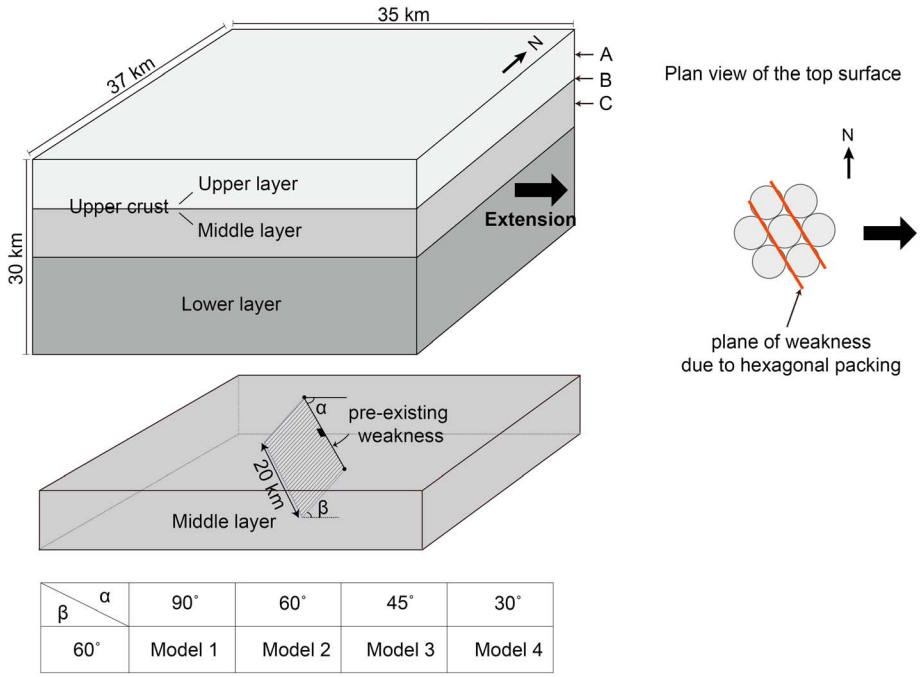

β \ α	90°	60°	45°	30°
60°	Model 1	Model 2	Model 3	Model 4

Figure 2. Cartoon of the three-layer model applied in this work. The upper and middle layers represent the upper crust, and the lower layer the firmoviscous lower crust. Marker horizons for discussion in the text are placed in the middle of the upper layer (A), at the interface between the upper and lower layers (B), and in the middle of the layer containing the preexisting weakness (C). The middle figure shows the middle layer with the location of the preexisting weakness. The lower table lists the four models with variable strike angles (α) of the preexisting weakness relative to the extension direction. The right cartoon shows the potential fault orientations that would be expected within the model owing to the hexagonal packing of the elements.

And the total force exerts on an element, *i*, in the lower crust is

$$F_{iL}^{\text{Total}} = \sum_{j=1,n}\left(F_{ijL}^{\text{elastic}} + F_{ijL}^{\text{viscous}}\right) + F_{iB} + F_{iG} + F_{iD} \tag{8}$$

Here *n* is the number of neighbors.

Extension of the crust is simulated by moving a rigid boundary wall (i.e., in the *y* component direction) in small increments over time, while the opposite wall is fixed. To maintain the boundary walls, elements at the extreme boundaries are constrained within the *x* component direction but are free to move in the *y* and *z* component directions. Calculations are carried out incrementally. At each time step, elements are moving to their new positions in the extension direction within the model, obeying equations of motion following Newtonian physics (Hardy & Finch, 2006). The new location of elements follows

$$Y_i(t+1) = Y_i(t) + \Delta Y\left(\frac{Y_i(t)}{Y_{\max}(t)}\right) \tag{9}$$

$Y_i\ (t+1)$ and $Y_i\ (t)$ are element locations at time steps $t+1$ and t, respectively, ΔY is the extension increment per time step, and $Y_{\max}\ (t)$ is the maximum length of the model in the extension direction at time step t.

Finite element modeling applied to investigate lithosphere-scale extension and rift evolution using thermomechanically coupled rheology noted the effect of temperature variations on structural styles in rifts (Behn et al., 2002; Cowie et al., 2005; Huismans & Beaumont, 2007). Cowie et al. (2005) suggested that basin-scale patterns of faulting are sensitive to the imposed thermal structure and horizontal strain rate. In our models, we do not consider the effect of temperature variations. We focus, however, on faults in the uppermost crust

Table 1
Rock Parameters Used for Each Layer in the Model

Rock parameters		Upper crust			Lower crust
		Upper layer	Middle layer	Preexisting weakness	
Element property	Elastic constant (K/K_c)	10×10^{10}	10×10^{10}	10×10^{10}	10×10^{10}
	Kelvin viscosity (η)				2.0×10^{11} Pa s
	Breaking threshold (r_b)	0.025–0.1 m.u.	0.05–0.1 m.u.	0.005–0.01 m.u.	
	Bond strength	2.5–10 GPa	5–10 GPa	0.5–1 GPa	
Assembly property	Poisson's ratio	0.25	0.25		
	Young's modulus (E)	108 GPa	108 GPa		

Note. Properties assigned to elements within the models dependent on layer (where m.u. represents model units). The value of bond strength is applied randomly at the beginning of the experiment to avoid preferentially oriented weakness in the models and is constant across the four models. Assembly property is the scaled macroscopic elastic property based on elastic constant of elements.

at a smaller scale than the aforementioned workers and consider that the influence of thermal variations in the crust is less significant at this scale.

2.2. Experiment Setup

Our model setup is a regular hexagonal packing of elements totaling 1,830,000. Each element is ~173 m in radius, which equals one model unit, and the model has initial dimensions of 213 × 201 × 173 (x,y,z) model units (m.u.) or 37 × 35 × 30 km (Figure 2). There is no inherent plane of weakness perpendicular to the extension direction due to the hexagonal packing of the media; therefore, faults opening in a N-S orientation are controlled by local stresses. The curvilinear nature of some fault paths in map view, however, may be controlled by the hexagonal packing of the elements and lead to 60° switching of fault strikes (Figures 1a and 2). For analysis purpose, the initial media is defined as 173 horizons. The model consists of three layers defined as lower, middle, and upper. The lower layer (15-km thick) represents the lower crust (Figure 2), the middle layer (7.5-km thick) represents basement, including a preexisting planar weakness whose tips terminate at the interface with the lower and upper layers (Figure 2). The upper layer (7.5-km thick) is considered to represent undeformed sediments overlying the preexisting weakness, without preferentially oriented weaknesses, and is defined to be thick enough to study the vertical growth pattern of faults. The physical parameters of each layer are shown in Table 1 and are chosen to be comparable to many natural examples and experiments scaled for investigation of rift basins (e.g., Place & Mora, 2001). In addition, the crust and mantle densities are 2,800 and 3,300 kg/m^3, respectively.

Four models are established to study variability in the influence of a preexisting fault on normal fault growth during extension due to a change in the strike angle (α) relative to the extension direction. In each model, the preexisting planar weakness is 20-km long, and its strike angle (α) relative to the extension direction ranges from 30° to 90° with a constant dip (β) is 60° (Figure 2). The length of the weakness is comparable to the natural examples of pre-Triassic faults reactivated during Middle-Late Jurassic in the northern North Sea rift (Whipp et al., 2014).

Extension is toward the east, in the y component direction within the model, while the western boundary wall is fixed (Figure 1a). The total run time is 50,000 time steps with a total extension of 25%, corresponding to an extension rate of 0.001 model units per time step. A time step equals 100 years, so the total run time is 5 Myr, which is within the general duration for a natural rift basin, being 1–15 Myr (Nicol et al., 1997). The extension rate equals 1.73 mm/year, corresponding to strain rates that vary from 1.585×10^{-15} s^{-1} to 1.288×10^{-15} s^{-1}, which are within the range of recorded strain rates in rift basins, being 1.0×10^{-16} to 4.0×10^{-14} s^{-1} (Kusznir & Park, 1987; Nicol et al., 1997).

2.3. Fault Analysis

At each time step, the horizontal and vertical offset between an element pair are stored. An individual fault is defined as a continuous alignment of elements that have similar dipping directions (westward or eastward), heaves (horizontal offset between element pairs in the extension direction) exceeding 50 m and positive throws (vertical offset). The value of heave is determined by testing to ensure that a defined fault excludes elements displaced by flexural rotation of horizons in hanging walls and footwalls (Finch & Gawthorpe,

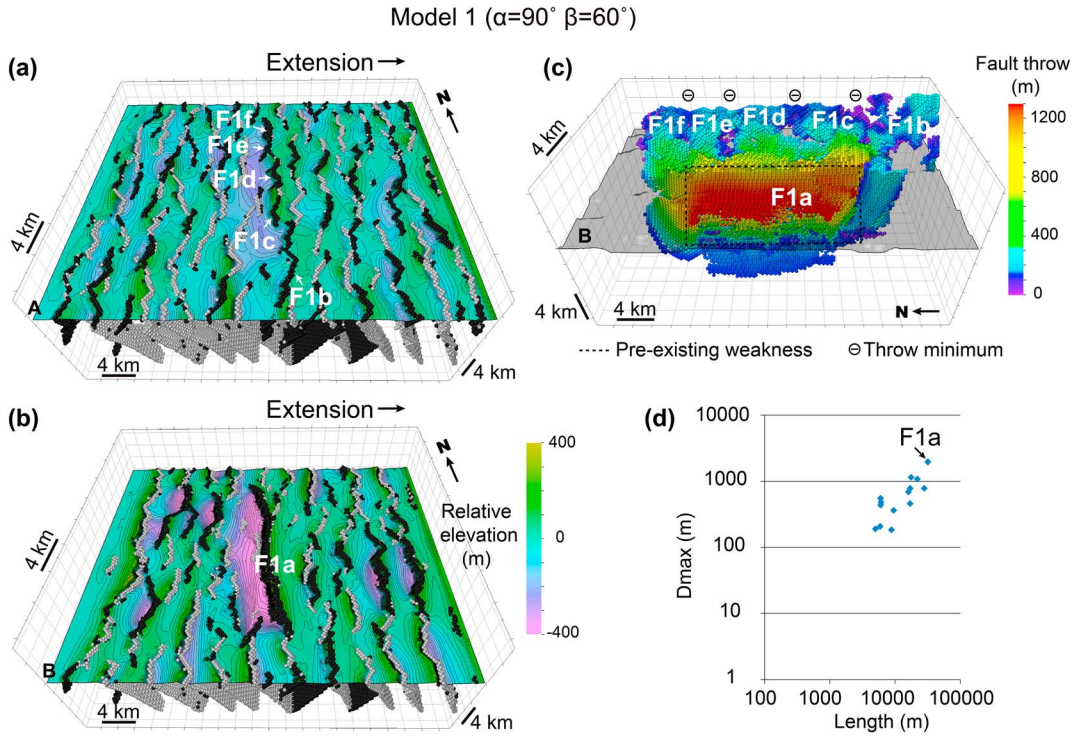

Figure 3. Fault geometry of Model 1. Faults observed relative to Horizon A (a) and Horizon B (b) at the final stage of extension (25%). West dipping faults are colored black, while east dipping faults are gray. (c) The throw projection on the fault plane related to the reactivated preexisting weakness (highlighted by the black dotted line) and nearby new faults, as viewed from the west, and relative to Horizon B at the interface between the upper and middle layers. (d) Plot of displacement maximum (D_{max}) against fault length (L) on Horizon B at 25% extension.

2017). Elements defining an individual fault are then extracted and visualized in Petrel, permitting analysis of fault geometry, interaction style, and their evolution in three dimensions.

Horizons from the middle (Horizon A [layer 153]) and base (Horizon B [layer 133]) of the upper layer and the middle (Horizon C [layer 113]) of the middle layer containing the preexisting weakness combined with fault traces are used to analyze fault length and strike in map view (Figure 2). In addition, throws recorded from elements constituting a fault are projected onto the strike section of the fault, from where throw variations are used to analyze fault growth history. Throw distribution is also used to investigate fault interaction styles in three dimensions. The value of displacement maximum (D_{max}) is approximated by the equation $D_{max} = 2 \times T_{max}/\sqrt{3}$, where T_{max} is the throw maximum, assuming faults dip at ~60° in general. Fault length (L) is the horizontal distance from the element with the maximum x value to that with the minimum x value along the strike.

3. Modeling Result

We divide the models into three sets according to the extent of reactivation of the preexisting weakness at 25% extension: (i) full reactivation, occurring in Models 1 and 2 ($\alpha = 90°$ and 60°); (ii) partial reactivation, represented by Model 3 ($\alpha = 45°$); and (iii) little or no reactivation, Model 4 ($\alpha = 30°$). The following sections describe each set of models, with a focus on differences in reactivation mode of the preexisting weakness and the resulting fault network in three dimensions, where the final fault geometries are presented before the fault network evolution.

3.1. Models 1 and 2: Full Reactivation

In Models 1 and 2, the preexisting weakness dips (β) at 60° and makes a strike angle (α) of 90° and 60° to the extension direction, respectively (Figure 2).

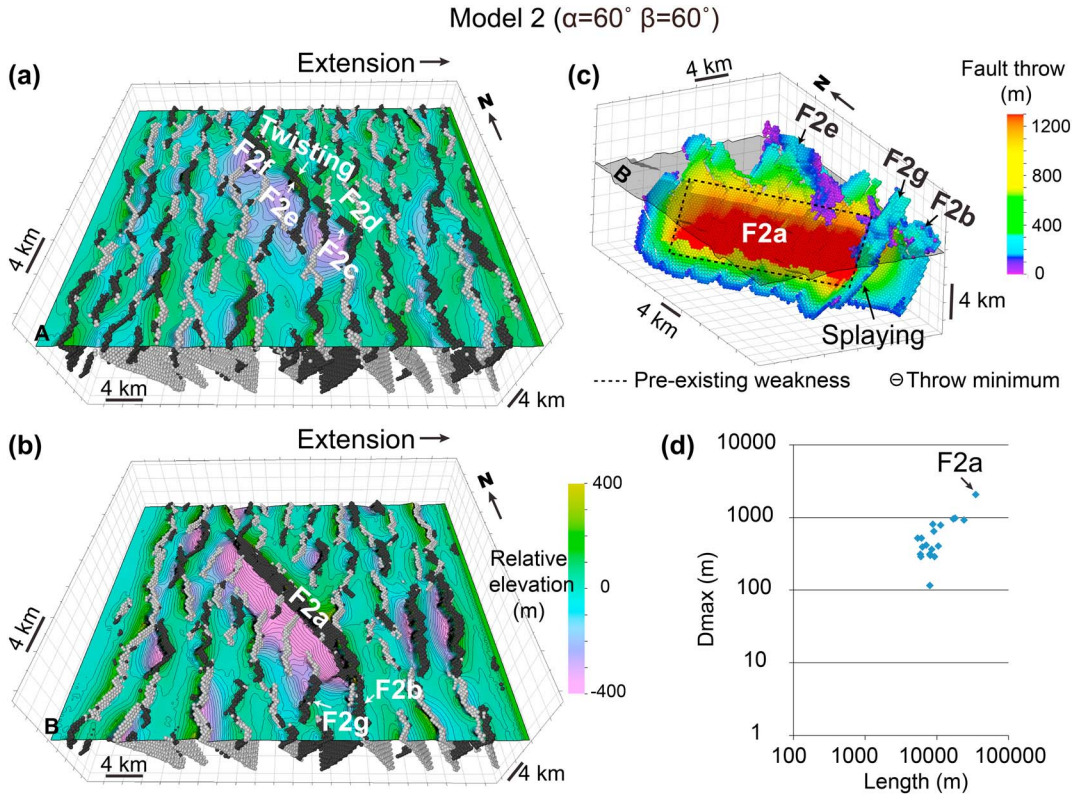

Figure 4. Fault geometry of Model 2. Faults observed relative to Horizon A (a) and Horizon B (b) at the final stage of extension (25%). West dipping faults are colored black, while east dipping faults are gray. (c) The throw projection on the fault plane related to the reactivated preexisting weakness (highlighted by the black dotted line) and nearby new faults, as viewed from the southwest, and relative to Horizon B at the interface between the upper and middle layers. (d) Plot of displacement maximum (D_{max}) against fault length (L) on Horizon B at 25% extension.

3.1.1. Final Fault Geometry

At 25% extension, the preexisting weakness in both models is fully reactivated, reaching a fault length of ˃20 km and generating a system of fringes (F1a–F1f in Figure 3 and F2a–F2f in Figure 4) in the cover. In addition, numerous smaller (<10-km long) extension-perpendicular faults dipping at ~60° develop away from the reactivated preexisting weakness, which show a characteristic curvilinear fault path related to the hexagonal packing of elements (Figures 3 and 4). However, the wavelength of the curvilinear path is limited (<2 km) compared to fault length.

In Model 1, fault F1 is 25–28 km in length and D_{max} ≈ 2,000 m and is related to reactivation of the preexisting weakness (Figure 3c). D_{max} of fault F1 occurs on the preexisting weakness (segment F1a) in the middle layer, from where displacement decreases radially (Figure 3d). In addition, a rectangular strain shadow zone (~25-km long and ~10-km wide), where few faults develop, exists symmetrically in the hanging wall and footwall of fault F1 at the base of the upper layer (Figure 3b). The upper part of fault F1 is composed of five 4- to 6-km-long fringes (F1b–F1f) separated by displacement deficits or minima along strike (Figure 3c). In map view, these fringes distribute in echelon pattern in the middle of the upper layer (Figure 3a). These observations suggest that the upper part of fault F1 forms by lateral linkage of several initial segments. Shorter (<10-km long) N-S striking faults also occur, oriented perpendicular to the extension direction, and dipping at ~60°.

In Model 2, fault F2 associated with the reactivation of the preexisting weakness is also 25–28 km in length with a D_{max} of ~2,000 m (Figure 4c). In the middle layer, fault F2 consists of a NNW-SSE striking segment (F2a) and a subsidiary N-S striking tail segment (F2b; Figure 4b). Also, its displacement decreases gradually from the major segment, F2a, toward its tips (Figure 4c). The upper tip line of the NNW-SSE striking segment is featured by a few *sawtooth* fringes in the upper layer. In addition, a twisting fault develops on top of each sawtooth fringe (e.g., F2c–F2f in Figure 4a). For example, fault segment F2e shows varying strike directions

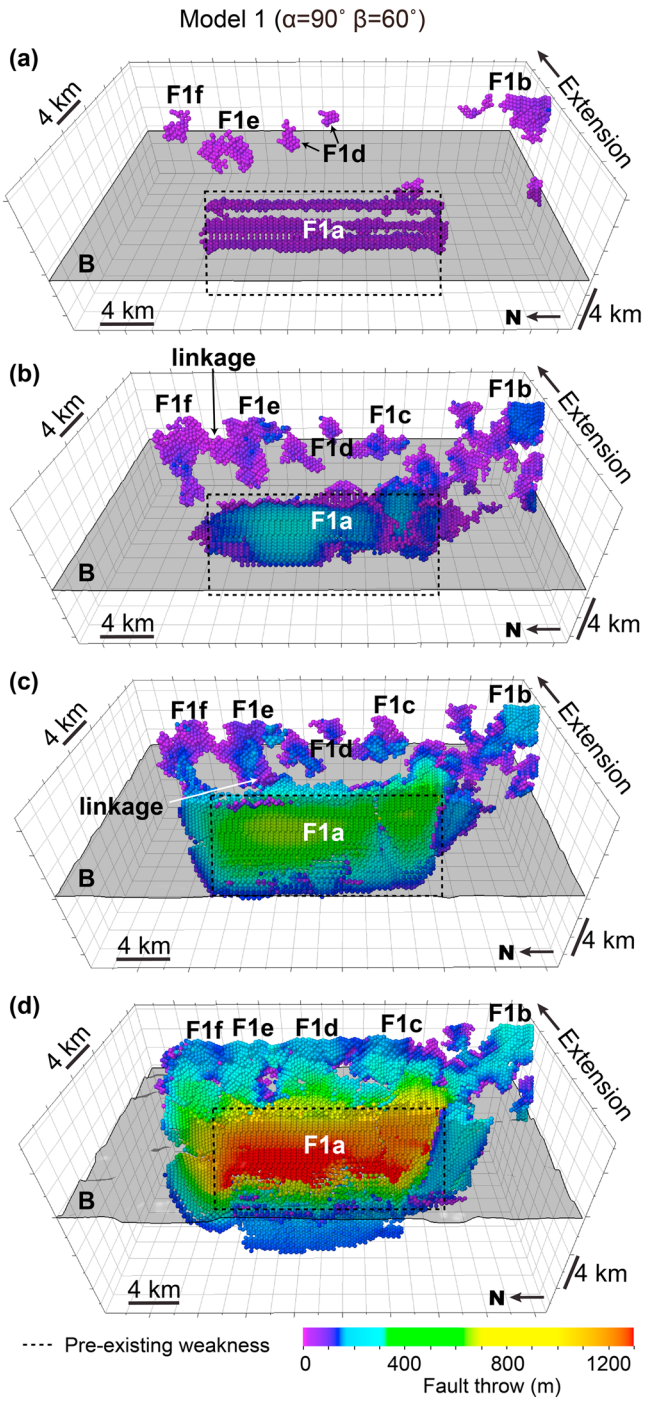

Figure 5. The 3-D representation of the reactivated preexisting weakness and its surrounding faults in Model 1 at four consecutive stages during extension viewed from the west at (a) 10%, (b) 15%, (c) 20%, and (d) 25% extension. The dotted black outline represents F1a, the preexisting weakness in Model 1. Horizon B, indicating the uppermost extent of the preexisting weakness, is included to aid visualization. The color bar represents fault throw in meters.

from N-S to NNW-SSE and then back to N-S (Figure 4a). Similar to Model 1, a rectangular and symmetric strain shadow zone (~25-km long and ~10-km wide) exists in the hanging wall and footwall of the reactivated fault (Figure 4b). Within the strain shadow zone, some newly developed faults strike at a high angle (>60°) to the major fault segment, F2a, forming a fault splay (e.g., F2g in Figure 4c). Hence, the reactivated fault in Model 2 has caused a change in the orientation of adjacent new faults from orthogonal to the extension direction to a high angle to the reactivated fault, with distances of up to 5 km away from the fault plane.

3.1.2. Fault Evolution

Between 0% and 10% extension, fault segments nucleate at various locations and depths in Models 1 and 2 (Figures 5a and 6a). Initially, fault segments F1a and F2a, relate to the reactivated preexisting weakness, both reach ~20 km in length in the middle layer, with $D_{max} \approx 30$ m (Figures 5a and 6a). No clear throw maximum is observed. The upper tip of F1a and F2a lies close to the top of the preexisting weakness, with one or more sawtooth fringes (Figure 5a). The lower tips do not extend to the bottom of the preexisting weakness. Other fault segments (F1b–F1f and F2b–F2f) are 2- to 5-km long in the upper layer, make a high angle to the extension direction and dip at 60° (Figures 5a, 6a, and 7a–7d), with D_{max} of ~30 m (Figures 5a and 6a). Hence, 50–80% of the preexisting weakness is reactivated at 10% extension. The preexisting fault is fully reactivated but with a relatively small D_{max}. The sawtooth fringes indicate that the reactivated portion of the preexisting weakness propagates upward faster at these locations. We suggest that this style of upward propagation is associated with heterogeneity in bond strength within the upper layer, which causes strain localization on certain locations of weak bonds above the reactivated fault.

Between 10% and 15% extension, the length of fault segments F1a and F2a increases from ~20 to ~23 km and D_{max} from ~30 to ~200 m. The sawtooth fringes propagate ~2 km into the upper layer, and the lower tip propagates closer to the base of the preexisting weakness (Figures 5b and 6b). As strain accumulates, a long and narrow (~23-km long and ~3-km wide) half-graben starts to develop in the hanging wall of F1a and F2a at the bottom of the upper layer (Figures 7f and 7h). Meanwhile, a rectangular strain shadow zone where few faults develop forms up to 5 km away from the plane of fault segment F2a, and faults in the strain shadow zone strike at a high angle to it (Figure 7h). Extension-perpendicular fault segments also increase their length from 2–5 to 5–8 km (Figures 7e and 7g) and D_{max} increases from ~30 to ~100 m (Figures 5b and 6b). Their lower tips propagate closer to the upper tips of F1a and F2a (e.g., F1e in Figure 5b). In addition, some of them link laterally or vertically (e.g., F1e and F1f in Figures 5b). Hence, this stage is mainly characterized by radial propagation of fault segments, and the reactivated fault starts to accommodate greater displacement than extension-perpendicular fault segments owing to its larger fault plane. In addition, the reactivated fault starts to exert an effect on the number and orientation of fault segments developing locally.

Between 15% and 20% extension, fault segments F1a and F2a increase their length from ~23 to ~26 km, D_{max} increases from ~200 to ~500 m, and their hanging-wall half-grabens (light purple color, ~ − 250-m elevation in Figures 7j and 7l) become more pronounced than other half-grabens in the models. The sawtooth fringes continue to grow upward and start to link vertically with extension-perpendicular fault segments (e.g., the

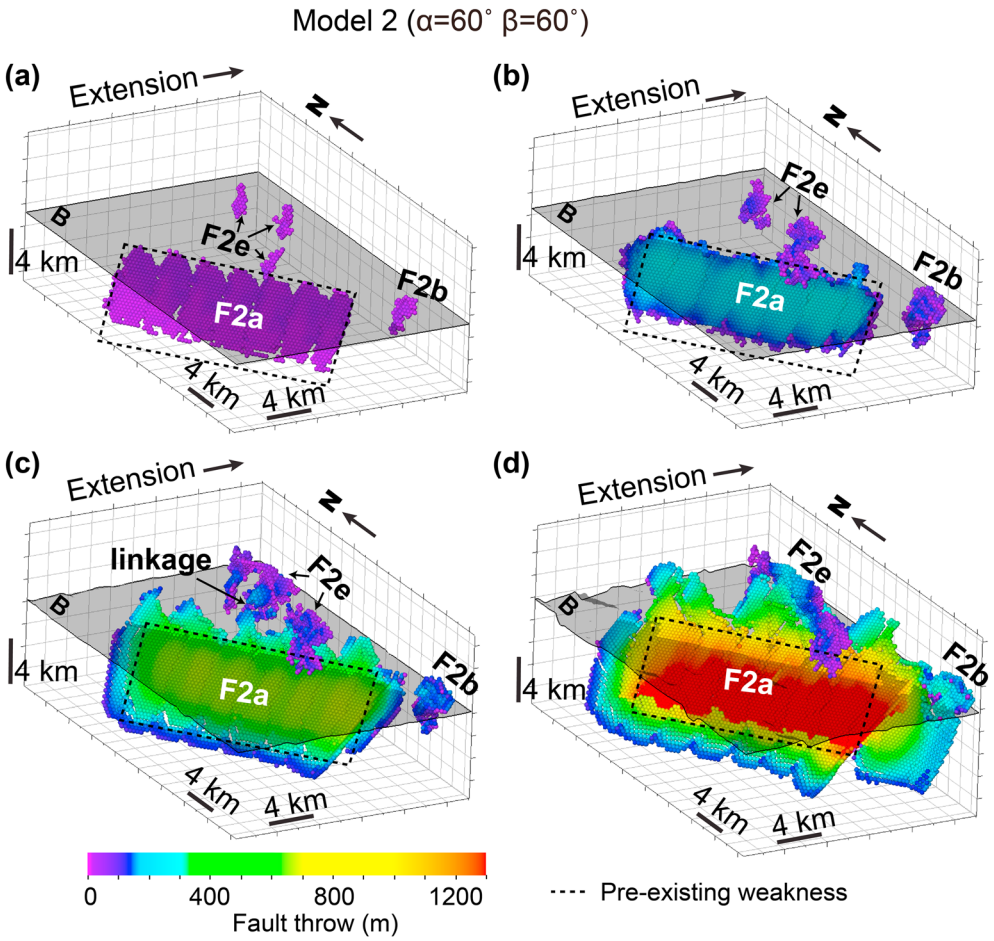

Figure 6. The 3-D representation of the reactivated preexisting weakness and its surrounding faults in Model 2 at four consecutive stages during extension viewed from the southwest at: (a) 10%, (b) 15%, (c) 20%, and (d) 25% extension. The dotted black outline represents F2a, the preexisting weakness in Model 2. Horizon B, indicating the uppermost extent of the preexisting weakness, is included to aid visualization. The color bar represents fault throw in meters.

linkage between F1a and F1e in Figure 5c). In addition, some small-scale half-grabens evolve in the hanging wall of fault segments F1b–F1f and F2b–F2f (light blue color, ~−150-m elevation in Figures 7i and 7k). This stage is characterized by further radial propagation of fault segments and linkage between the reactivated fault and extension-perpendicular fault segments.

Between 20% and 25% extension, fault segments F1a and F1b–F1f link to form a continuous fault system F1 (Figure 5d). D_{max} of the fault system F1 is still located at the preexisting weakness, with some displacement minima existing at points of lateral linkage between fault segments F1b–F1f in the upper layer (Figure 5d). In contrast, the areas of vertical linkage have a greater displacement than the original cores of these segments (Figure 5d). In Model 2, similar characteristic of displacement distribution is observed on fault F2. In addition, linkage between the sawtooth fringes of F2a and new fault segments create twisting fault geometries in three dimensions (e.g., F2e in Figures 6d and 7o, see also Figure 8 in Deng, Gawthorpe, et al., 2017). Hence, linkage between the reactivated fault and extension-perpendicular fault segments is more significant during this stage. Following linkage, the original displacement maximum at the center of extension-perpendicular fault segments is overprinted, owing to the dominance of the reactivated fault. In addition, linkage between the reactivated fault oblique to the extension direction and extension-perpendicular fault segments forms a non-planar fault that is locally twisted into a NNW-SSW trend corresponding to the preexisting fault.

3.2. Model 3: Partial Reactivation

Here, the preexisting weakness has a strike angle (α) of 45° relative to the extension direction and is dipping (β) at 60° (Figure 2).

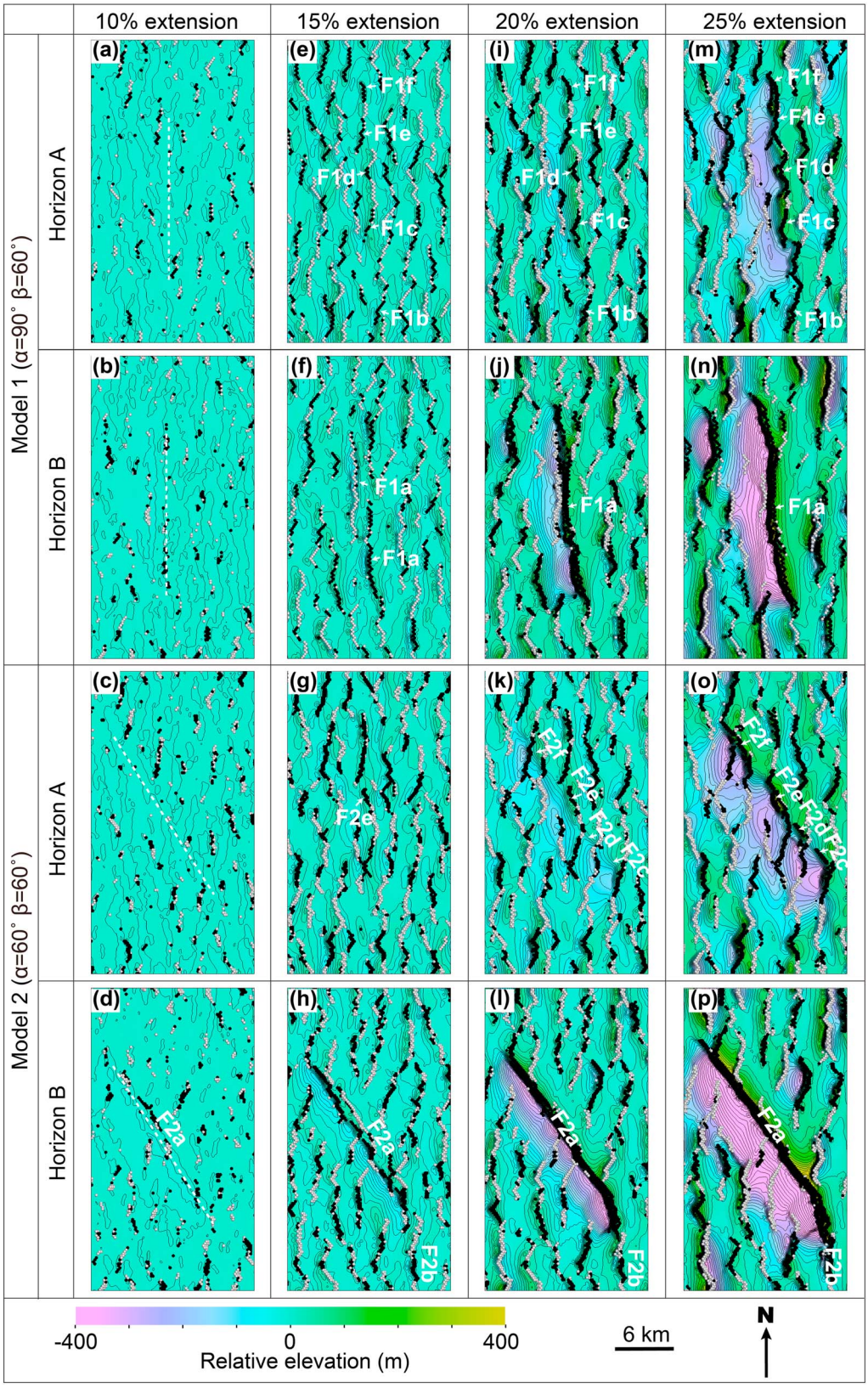

Figure 7. (a–p) Surface maps of Horizons A and B in Models 1 and 2 at 10%, 15%, 20%, and 25% extension. Black lines show west dipping faults, while gray lines show east dipping faults. The white dashed lines in (a)–(d) represent the length and orientation of the preexisting weakness. The color bar represents relative elevation.

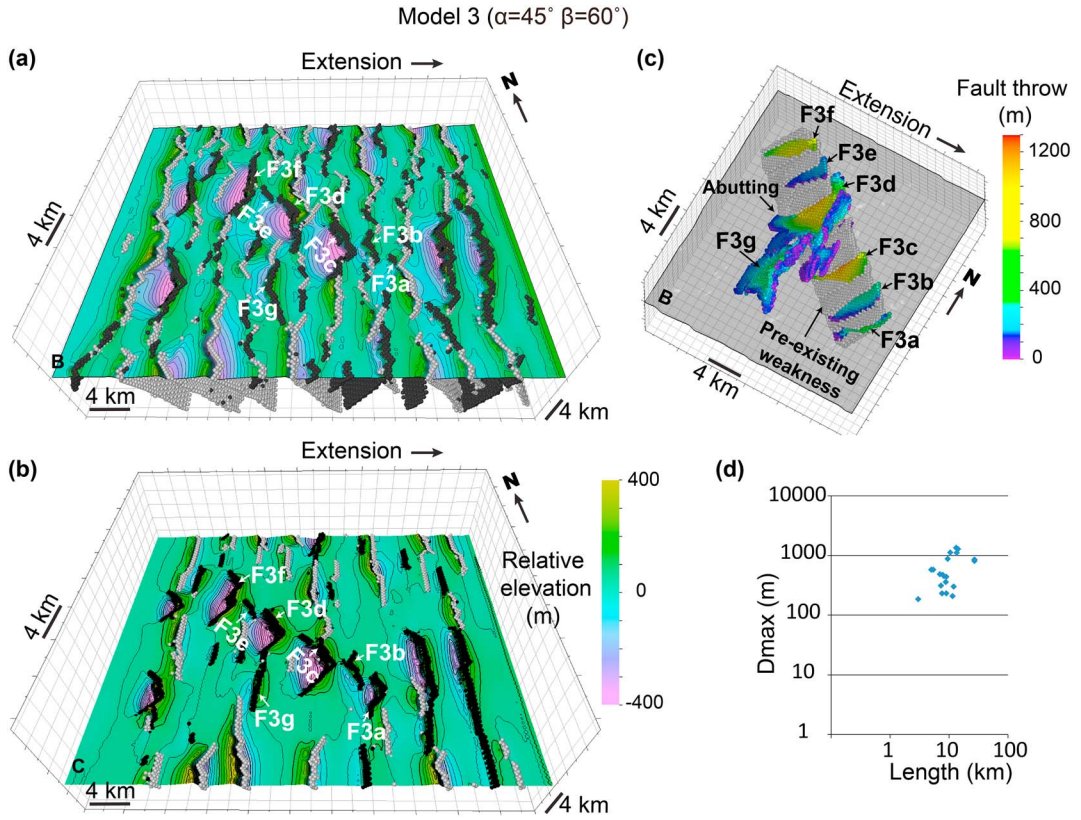

Figure 8. Fault geometry of Model 3. Faults observed relative to Horizon B (a) and Horizon C (b) at the final stage of extension (25%). West dipping faults are colored black, while east dipping faults are gray. (c) The throw projection on the fault plane related to the reactivated preexisting weakness and nearby new faults, as viewed from the southeast, and relative to Horizon B at the interface between the upper and middle layers. (d) Plot of displacement maximum (D_{max}) against fault length (L) on Horizon B at 25% extension.

3.2.1. Final Fault Geometry

In Model 3, six isolated segments (F3a–F3f) originate along the plane of the preexisting weakness and accumulate significant displacement, being 1–4 km in length with a D_{max} ~1,200 m (Figure 8). For example, fault segment F3d has two differently striking segments in the middle layer. One is ~3-km long, NW-SE striking and related to the preexisting weakness; the other is also ~3-km long, NE-SW striking and perpendicular to the preexisting weakness (Figures 8b and 8c). D_{max} of F3d occurs on the NW-SE striking segment, from where displacement decreases radially (Figure 8c). Toward the south, the NE-SW striking segment of F3d links laterally with the N-S striking F3g fault segment, showing twisted fault geometry in the middle layer (F3g in Figure 8c). Therefore, the preexisting weakness in Model 3 is not reactivated as a continuous structure but as several short and isolated fault segments along strike. The preexisting weakness also influences the strike of new faults that develop perpendicular to it in the middle layer, for distances of up to 3 km from the preexisting weakness.

3.2.2. Fault Evolution

Between 0% and 10% extension, no fault segments initiate on the plane of the preexisting weakness in Model 3 (Figure 9a). However, extension-perpendicular fault segments initiate away from the preexisting weakness, being up to 3-km long and dipping at ~60° (Figures 9a and 10a). D_{max} of these fault segments is approximately 30 m. Hence, this stage is characterized by scattered fault segment nucleation but not localized on the preexisting weakness.

Between 10% and 15% extension, some isolated fault segments nucleate on the preexisting plane of weakness, being ~3-km long and at 60° dip, developing a D_{max} of ~100 m (e.g., F3d in Figure 9b). The length of extension-perpendicular fault segments increases from ~3 to ~8 km as some link laterally, and their D_{max} increases from ~30 to ~100 m (e.g., F3g in Figures 9b and 10b). Hence, some small fault segments with

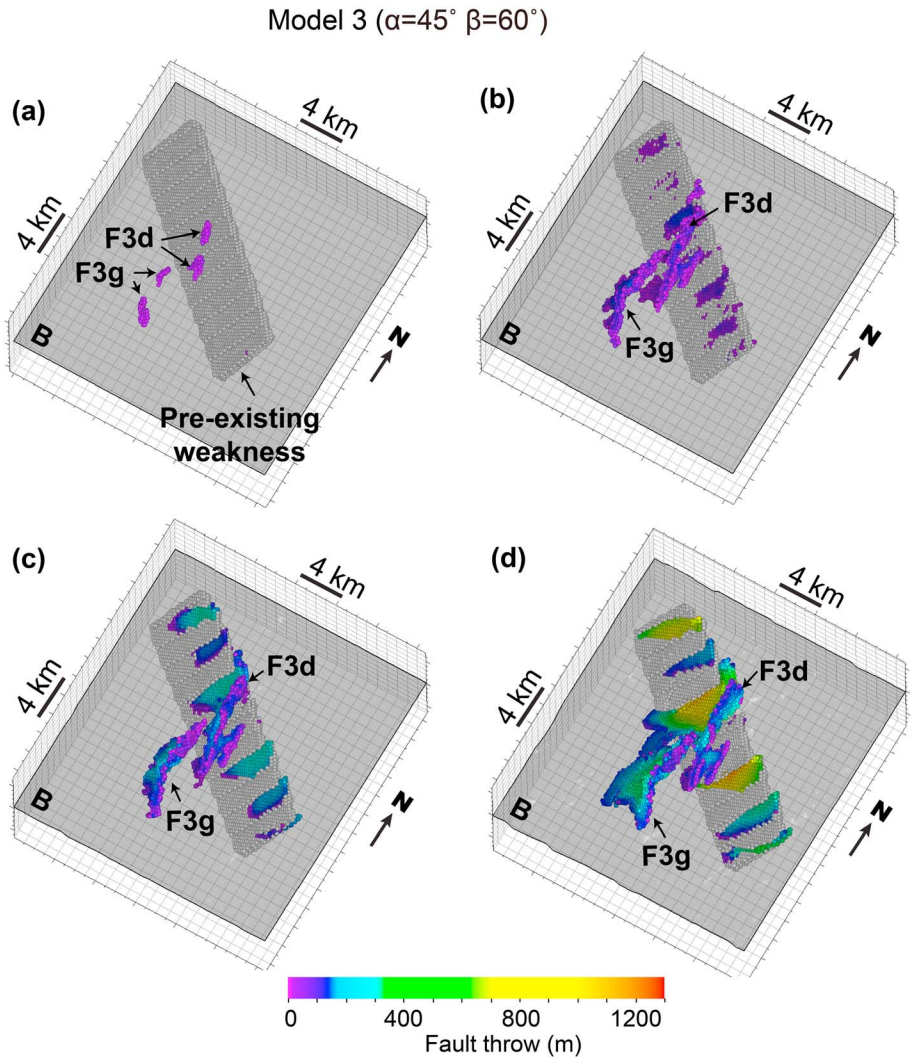

Figure 9. The 3-D representation of the preexisting weakness (gray) and its surrounding faults in Model 3 at four consecutive stages during extension viewed from the southwest at (a) 10%, (b) 15%, (c) 20%, and (d) 25% extension. Horizon B, indicating the uppermost extent of the preexisting weakness, is included to aid visualization. The color bar represents fault throw in meters.

length and displacement similar to extension-perpendicular segments initiate on the preexisting fault during this stage (Figures 9b and 10b). The small fault length and displacement of the reactivated fault in Model 3 contrast with Models 1 and 2 where the reactivated fault has a D_{max} of ~200 m at this stage and becomes the dominant fault (fault segments F1a and F2a in Figures 5b and 6b). This difference must be caused by the different orientation of the preexisting fault relative to the extension direction, since all other parameters are the same.

Between 15% and 20% extension, the segments initiating on the preexisting weakness in Model 3 increase in length from ~3 to ~5 km (Figure 10c), and D_{max} increases from ~100 to ~300 m (Figure 9c). The extension-perpendicular segments show similar evolution (e.g., F3g in Figures 9c and 10c). Thus, this stage is mainly characterized by continued fault propagation.

Between 20% and 25% extension, fault segment F3d laterally propagates perpendicularly out of the preexisting weakness in the middle layer, generating a new segment of ~3 km in length (Figure 9d). In addition, this segment (F3d) laterally links with segment F3g to the south, forming a twisted fault geometry in the middle layer (Figure 9d and 10d). D_{max} of fault segment F3d increases from ~300 to ~800 m and is still located at the preexisting weakness (Figure 9d).

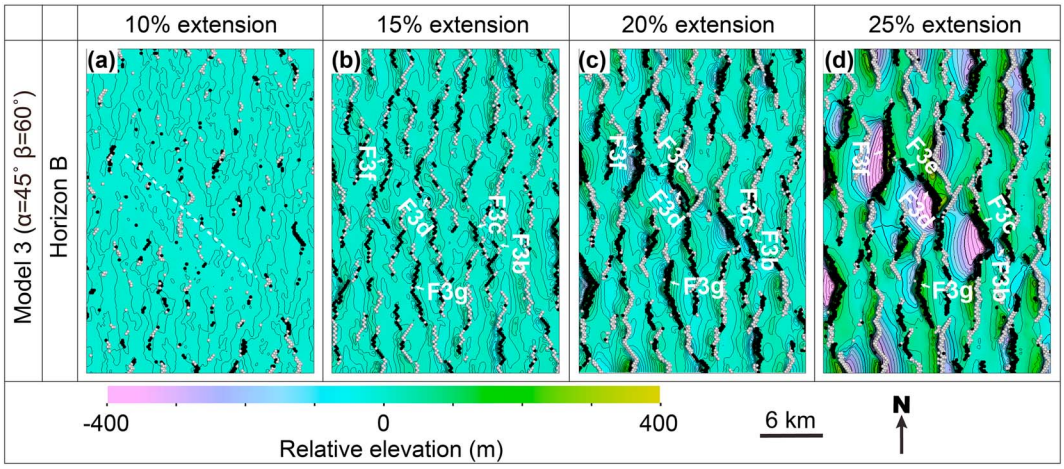

Figure 10. Surface maps of Horizon B in Model 3 at four consecutive stages of extension representing: (a) 10%, (b) 15%, (c) 20%, and (d) 25%. Black lines show west dipping faults, while gray lines show east dipping faults. The white dashed line in (a) represents the length and orientation of the preexisting weakness, and the color bar represents relative elevation.

3.3. Model 4: No Reactivation

In Model 4, the preexisting weakness has a strike angle (α) of 30° relative to the extension direction and a dip (β) of 60° (Figure 2).

3.3.1. Final Fault Geometry

At 25% extension, faults developing in Model 4 have an average N-S strike, perpendicular to the extension direction (Figure 11a). Extension-perpendicular faults offset the plane of the preexisting weakness (Figure 11b). For example, fault F6a cuts across the preexisting weakness at the branch line. The purple color on the preexisting weakness near the branch line is due to block rotation in the hanging wall of fault F6a. Throw of fault F6a at the branch line is not zero (green color), so its lower tip is hidden in the footwall of the preexisting fault. Therefore, the preexisting weakness is not reactivated and is crosscut and offset by extension-perpendicular faults (Figure 11b).

3.3.2. Fault Evolution

Evidence on Figures 12 and 13 shows that extension-perpendicular fault segments nucleate and grow radially in the upper and middle layers of Model 4, followed by lateral and vertical linkage to form bigger

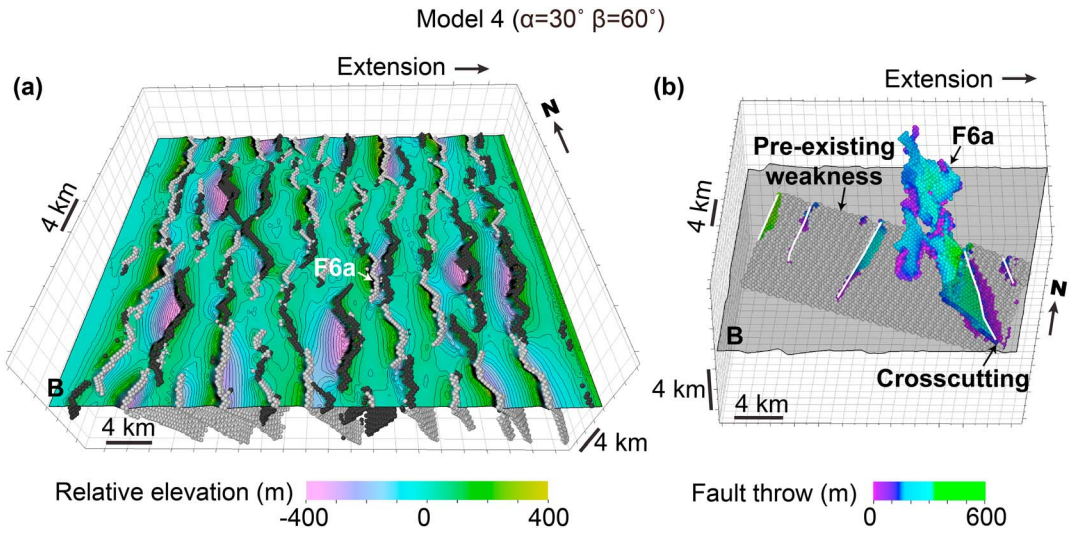

Figure 11. Fault geometry of Model 4. (a) The faulted Horizon B at the final stage of extension (25%). Black lines show west dipping faults, while gray lines show east dipping faults. (b) The throw distribution on the preexisting weakness and nearby new faults at 25% extension relative to Horizon B. White lines are branch lines between the preexisting plane of weakness and new faults, and throw on the preexisting planar weakness shows the offset of the plane by those faults.

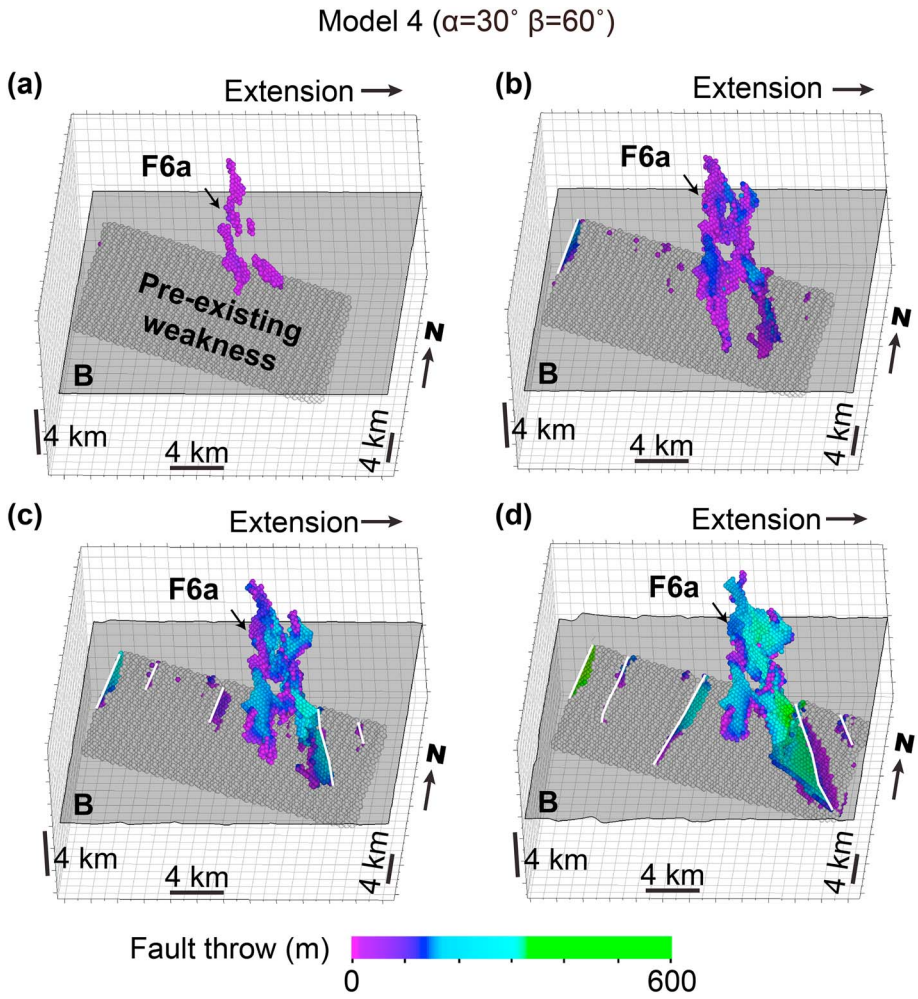

Figure 12. The 3-D illustration of the preexisting weakness and its surrounding faults viewed from the south in Model 4 at 10% (a), 15% (b), 20% (c), and 25% (d) extension relative to Horizon B. The color bar represents fault throw in meters. White lines are branch lines between the preexisting plane of weakness and new faults, and throw on the preexisting planar weakness shows the offset of the plane by those faults.

faults over time. For instance, some fault segments of fault F6 nucleate randomly in the upper layer but not on the preexisting fault (Figure 12). They link, propagate downward, and offset the preexisting fault as strain accumulates (Figure 12). Half-grabens in their hanging walls show no significant elevation change (Figure 13). The preexisting weakness remains inactive through the extension but is crosscut and offset by extension-perpendicular faults when extension exceeds 20% (Figure 12). Therefore, the effect of the preexisting weakness on the growth of new faults is absent in this model. New faults generally grow by radial propagation and linkage of isolated fault segments away from the preexisting weakness, which is quite similar to the ideal three-stage model for fault growth in a homogeneous crust during a single rift phase (Cowie et al., 2000, 2005; Gawthorpe et al., 2003; Gawthorpe & Leeder, 2000; McLeod et al., 2000; Meyer et al., 2002).

4. Discussion

We have examined the variety in three-dimensional fault geometry and the evolution of a normal fault network over a weak planar preexisting fault with various strike angles relative to the extension direction by means of numerical modeling. The modeling results confirm the general notion that the reactivation pattern of a preexisting fault and its effect on the adjacent fault network is greatly related to its strike angle (α) relative to the extension direction. In particular, a preexisting fault with a dip of 60° is fully reactivated for $\alpha \geq 60°$, partly reactivated for $\alpha = 45°$ and not reactivated for $\alpha = 30°$ (Figure 14). We also observe that newly

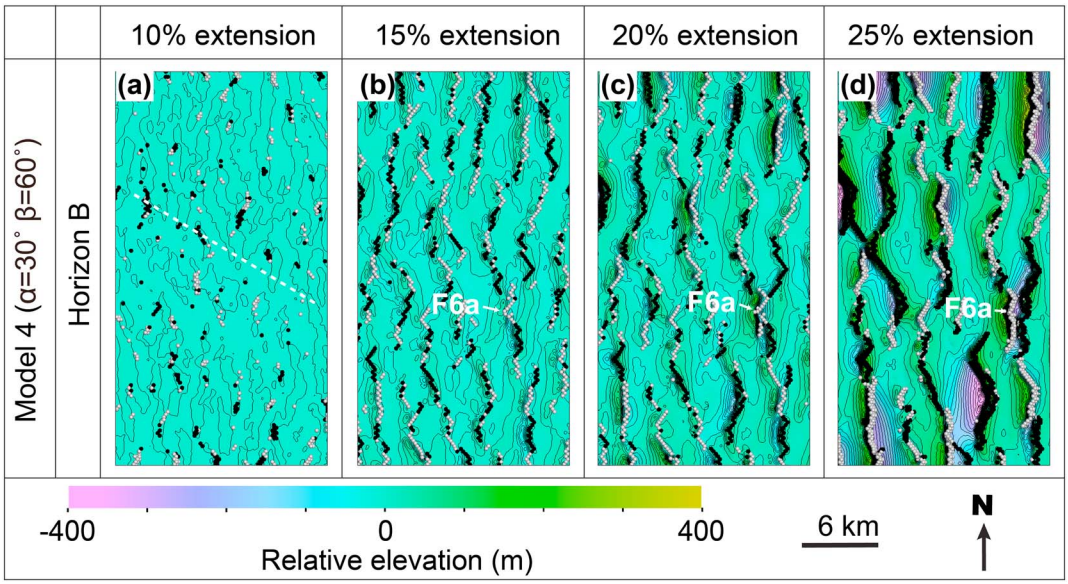

Figure 13. Surface maps of Horizon B in Model 4 at four consecutive stages of extension representing: (a) 10%, (b) 15%, (c) 20%, and (d) 25%. Black lines show west dipping faults, while gray lines show east dipping faults. The white dashed line in (a) represents the length and orientation of the preexisting weakness and the color bar represents relative elevation in meters.

formed faults nucleate independently from the preexisting fault as isolated structures both in the upper and middle layers of all models (Figures 7–13). Some nearby newly formed faults gradually propagate toward the reactivated fault and subsequently link, forming a continuous fault system and various fault interaction styles.

4.1. Reactivation Modes of a Preexisting Fault

Physical analog modeling of two phases of extension suggests that the reactivation of first-phase faults is to be expected for angles as high as 45° between the two extension directions (Bonini et al., 1997; Henza et al., 2010, 2011; Keep & McClay, 1997). Henza et al. (2010) used scaled analog models (wet clay) to study normal fault development during two phases of extension whose directions differ by up to 45°. They observed that preexisting faults were reactivated during the second phase of extension, along with the development of new normal faults. Similarly, the reactivation of first-phase faults has been found during the second rift phase in parts of the northern North Sea rift where there was a rotation in the local extension direction by 30–45° between the two rift phases (Davies et al., 2001; Deng, Gawthorpe, et al., 2017; Færseth, 1996; Færseth et al., 1997). In contrast, Fazlikhani et al. (2017) observed that prerift structures striking close to the extension direction of rifting on the Måløy Slope were less likely to be reactivated than those more favorably oriented in the Horda Platform and East Shetland Basin, northern North Sea. Therefore, our modeling results are consistent with observations from physical analog models and natural rifts and support the conclusion that reactivation of a preexisting fault is more likely when it makes a high angle to the extension direction. Furthermore, we find that the reactivation of a preexisting fault is characterized by three different modes: full, partial, and no reactivation (Figures 14 and 15).

The modeling results indicate that the preexisting fault evolves from initially isolated fault segments to a connected fault system. More specifically, the evolution of a fully reactivated preexisting fault and nearby new faults involves three stages (Figure 15a). Initially, the preexisting fault is reactivated, while newly formed faults initiate independently at shallower levels in their early history. Thereafter, the reactivated fault propagates upward and new faults propagate downward as strain accumulates. And finally, the reactivated fault links vertically with overlying new faults later in their growth history, forming a continuous fault system. For the case of a partially reactivated preexisting fault, the reactivated section is not likely to propagate through the entire upper layer owing to its small size but rather affects only the lower part of the upper layer (Figure 15b). The reason that the preexisting fault and new faults develop an initially decoupled pattern is related to the large thickness of the overburden in the models. Such decoupling is common where layers of mechanically contrasting properties exist (e.g., salt-involved decoupling; Jackson & Rotevatn, 2013), but

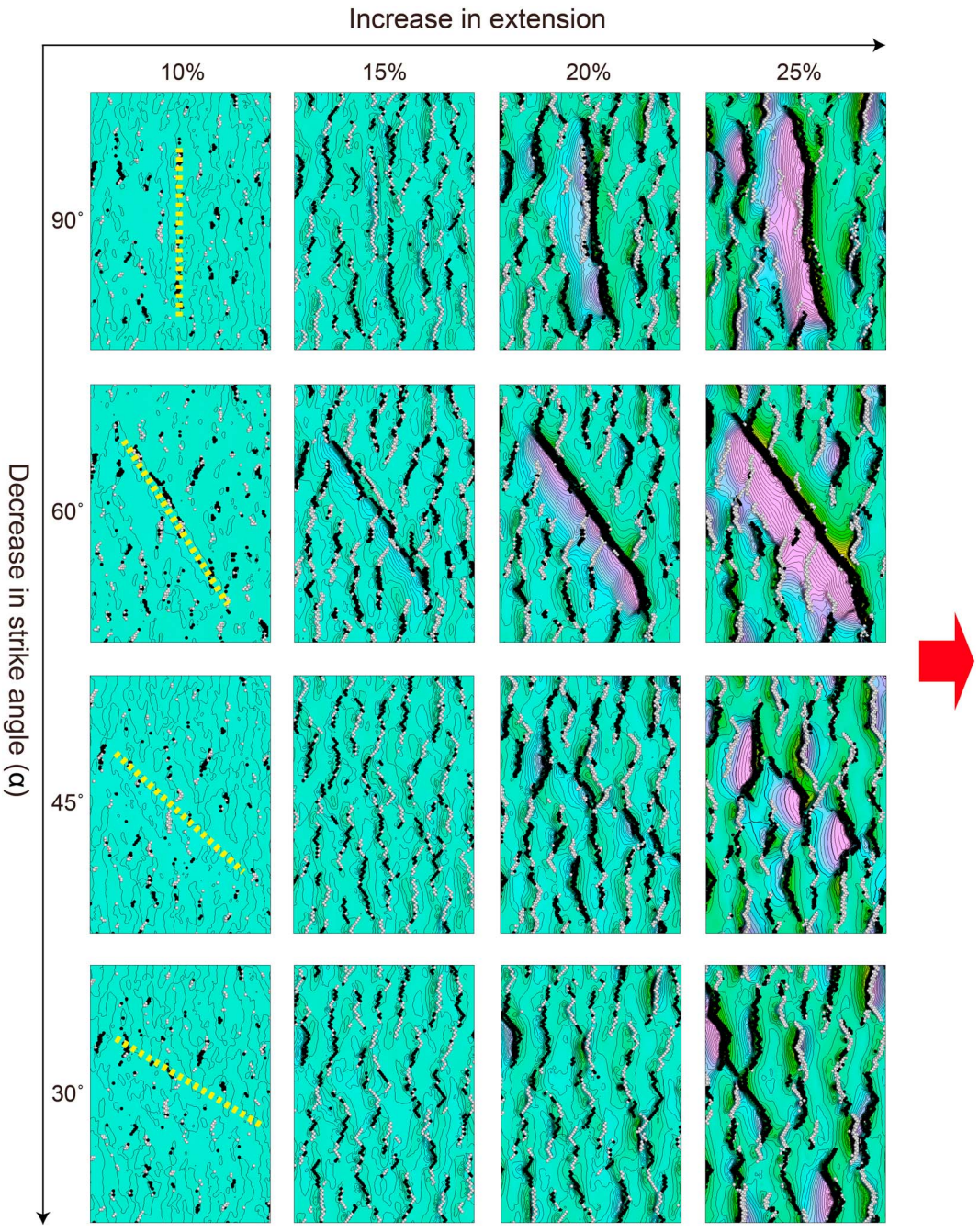

Figure 14. Summary of faulting observed on Horizon B for the four models showing the difference in fault reactivation during extension related to the strike angle (α) relative to the extension direction (red arrow). Black lines show faults dipping left, while gray lines show faults dipping right. The yellow dashed lines at 10% extension represent the length and orientation of the preexisting weakness.

in our case there are no real extremes in the stratification of strength of the model. We suggest that the succession overlying the preexisting fault is thick (7.5 km) enough that it fails independently in the uppermost layer during the imposed uniform extension. Another possible reason is the element properties within the overburden, where the bond strength is randomly assigned. In other words, there are inherent weaknesses in the upper layer that are of similar *strength* to those on the basement fault. As such, there will be localization on these weaknesses at similar times as the preexisting weakness and so faults will form in both the upper and lower layers coincidentally. Therefore, the combination of a thick overburden

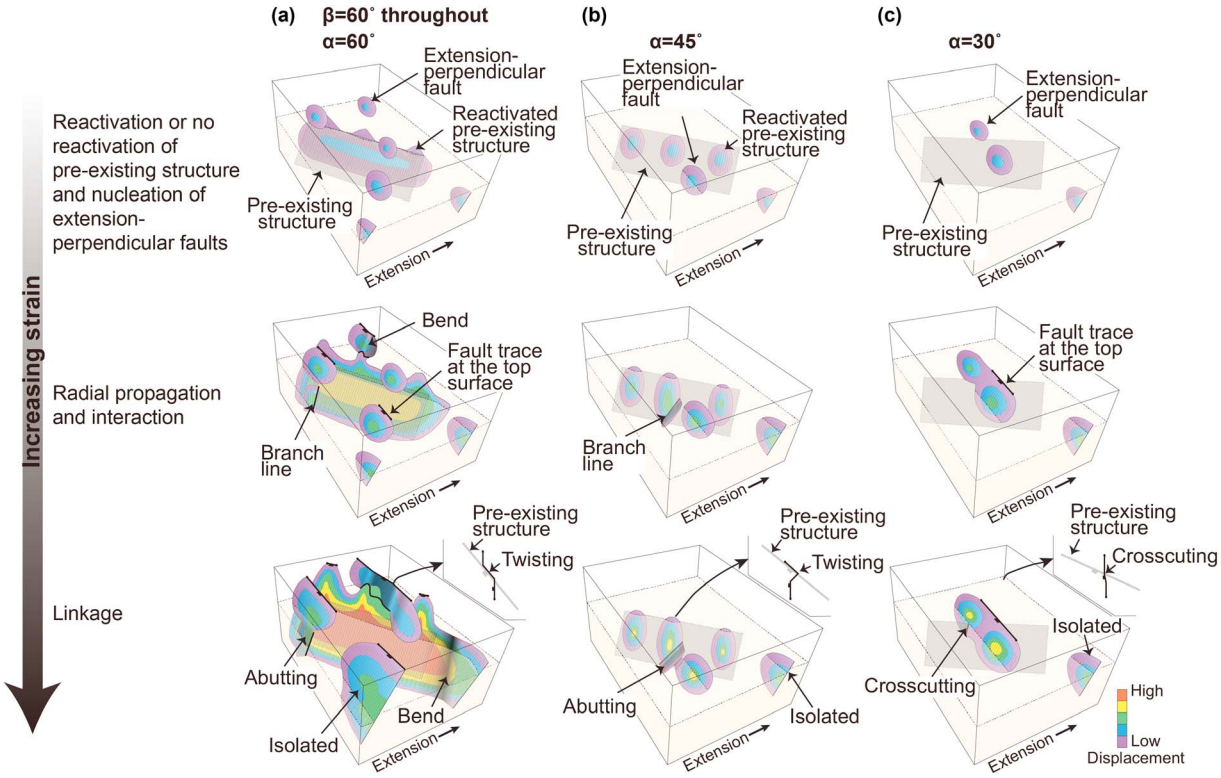

Figure 15. Summary figure showing the difference in fault evolution and fault interaction styles developing during oblique extension where α, the strike angle of the preexisting weakness to the extension direction, is (a) 60°, (b) 45°, and (c) 30°. The insets in the top right corner of the bottom three figures show fault interaction between the preexisting fault and extension-perpendicular faults in map view. Black fault traces indicate the surface expressions of faults. The color bar reflects fault displacement.

and its heterogeneity in mechanical strength leads to decoupled deformation between the upper and middle layers of our models.

4.2. Impact on Adjacent Fault Development

We observe that a strain shadow zone forms around the reactivated fault, for instance, around faults F1 and F2 in Figure 7. In this zone, fault density is significantly decreased as compared to surrounding areas, reflecting strain localization on the reactivated fault. In addition, the size of the strain shadow zone shows a decreasing trend with the strike angle of the preexisting fault, so that the size of the strain shadow zone is proportional to the reactivation potential of the preexisting fault. Ackermann and Schlische (1997) suggested a stress-reduction shadow, similar to the strain shadow zone in this study, in the vicinity of master faults where the nucleation of smaller faults is retarded. They collected the length and displacement data of faults that have a well-defined stress-reduction shadow and found the size of the stress-reduction shadow to increase linearly with fault displacement. Our modeling results demonstrate similar characteristics regarding the size of the strain shadow zone versus fault size (fault length and displacement). Therefore, we expect that easily reactivated major faults alter the strain distribution through such a strain shadow because of their large size early in their growth history.

We also find that a reactivated fault influences the strike orientation of adjacent new faults. With large α (=60°), new faults develop in the strain shadow zone of the reactivated fault at high angles to the reactivated fault (Figure 4a). Also, the reactivated segments of the preexisting weakness propagate outward in a direction perpendicular to the preexisting plane of weakness with an intermediate α (=45°) and large β (=60°), in distances of up to 5 km (Figure 8j). Henza et al. (2010) studied fault evolution during two phases of noncoaxial extension by using clay analog models and observed that second-phase faults were initially orthogonal to preexisting faults and became approximately orthogonal to the second-phase extension direction as they propagated away from preexisting faults. Second-phase faults forming perpendicular to a preexisting fault reflect that the preexisting fault perturbs the local extension direction (Homberg et al., 2004, 1997).

Hence, the development of newly formed faults striking approximately perpendicular to a reactivated preexisting fault in its vicinity indicates that the preexisting fault reactivates obliquely.

In addition, a preexisting fault influences fault length, depending on the strike of the preexisting fault relative to the extension direction. With a large α ($\geq$60°), the preexisting fault reactivates to form a fault whose length equals that of the initial preexisting fault during the early growth history (Figure 15a). With an intermediate α (=45°), however, the preexisting weakness partly reactivates and favors the development of several isolated fault segments within the preexisting plane of weakness, each with a length similar to that of the extension-perpendicular fault segments (Figure 15b). Such variations in the reactivation and growth pattern of a preexisting weakness represent two end-members of the fault growth model: (i) the isolated fault model (e.g., Baudon & Cartwright, 2008; Cartwright et al., 1995; Contreras et al., 2000; Dawers & Anders, 1995; Fossen & Rotevatn, 2016; Huggins et al., 1995; Jackson et al., 2002; Mansfield & Cartwright, 1995; McLeod et al., 2000; Morley, 1999; Morley et al., 1990; Rykkelid & Fossen, 2002; Schlische & Anders, 1996; Trudgill & Cartwright, 1994; Walsh et al., 2003; Walsh & Watterson, 1988; Young et al., 2001) and (ii) the coherent fault model (Childs et al., 1995; Giba et al., 2012; Schöpfer et al., 2006; Walsh et al., 2003, 2002). The reactivation of the preexisting weakness with an intermediate α (=45°) is in accordance with the isolated fault model, where a few short, isolated segments nucleate on the preexisting plane of weakness, and then propagate, interact, and link with extension-perpendicular fault segments over time. In contrast, the reactivation and further growth of the preexisting weakness with a large α ($\geq$60°) resemble the coherent fault model, where a reactivated preexisting weakness reaches its near-constant fault length relatively early in its growth history, followed by a long period of displacement accrual without significant increase in length owing to interaction between fault segments. The difference in the growth pattern of a preexisting weakness owing to varying strike angles indicates that both the isolated and coherent fault models are applicable to the reactivation of a preexisting fault. A similar implication was also outlined in Jackson and Rotevatn (2013).

The impact of a preexisting fault on fault displacement is indicated by displacement enhancement on fault segments that link to the reactivated fault with a large α ($\geq$60°; Figure 15a). For example, the final displacement distribution of the fault system F1 in Model 1 (α = 90°) has a radially decreasing trend from the core, segment F1a, to segments F1b–F1f (Figure 3c). If fault growth history is not considered, the final displacement distribution on fault system F1 may be misinterpreted as a result of upward propagation of the fringes from the core F1a alone. Indeed, the evolution of fault system F1 also involves vertical linkage of the fringes of F1a and the concurrent fault segments F1b–F1f that nucleate separately in the upper layer. In addition, the existence of several displacement minima in the upper part of fault system F1 indicates that this part consists of several fault segments that are initially isolated and then laterally linked, thus argues against the model of upward propagation (Figure 3c). The modeling results show that the reactivated fault enhances the displacement of the fault segments that link to it, which masks the initial displacement distribution that characterizes segmentation of a large fault system. This effect on fault displacement implies that using the final displacement distribution or D-L plots to interpret the evolution of fault systems needs to consider the influence of preexisting faults. Otherwise, it may lead to a misleading interpretation of the underlying dynamics. Displacement enhancement is also found in Model 2 (α = 60°; see also Deng, Gawthorpe, et al., 2017) but not in other models where the preexisting weakness ($\alpha < 60°$) does not control strain localization during extension. Therefore, a major fault may have a significant effect on the final displacement distribution of faults linking to it.

4.3. Variation in Fault Interaction Styles and Implications

Since the impact of a preexisting fault on the geometry of adjacent new faults depends on its orientation relative to the extension direction, the resultant fault interactions in our models have different styles as well. In the model with a large α (=60°), fault interaction styles include: (i) splaying, where new faults nucleate at and then propagate away from the reactivated preexisting fault (e.g., F2 g in Figure 4c, see also Nixon et al., 2014); and (ii) twisting, where sawtooth fringes of the reactivated fault link vertically and laterally with extension-perpendicular faults in the upper layer (e.g., F2e in Figure 6). Twisting interactions also develop in the model with an intermediate α (=45°) but mainly in the middle layer (e.g., F3d and F3g in Figure 8c). In the model with a small α (=30°), extension-perpendicular faults crosscut and offset the preexisting fault (e.g., F6a in Figure 11b). Hence, there is a shift from splaying and twisting to crosscutting interactions as the strike angle of the preexisting fault relative to the extension direction decreases, along with a decreasing influence of the preexisting fault.

Fault interaction styles were also investigated in three dimensions via analysis of fault displacement distribution on strike projections in multiphase rift basins. For instance, Duffy et al. (2015) found that NW-SE striking second-phase faults terminate against a larger N-S striking first-phase fault in the northern North Sea rift. Based on final displacement distribution, second-phase faults were interpreted to nucleate either on first-phase faults and then propagate outward or away from and then terminate against first-phase faults. A difference in the local extension direction of 30–45° during the two rift phases was suggested, corresponding to our models with an α of 45–60°. Crosscutting interaction has also been identified in the Jeanne d'Arc rift basin of offshore Newfoundland (Enachescu, 1987; Sinclair, 1995a, 1995b), where first-phase N-S striking faults are crosscut and offset by second-phase E-W striking faults. This crosscutting pattern and its high angle between the two extension directions is similar to our model with a small α (=30°).

These observations from multiphase rifts suggest a shift from splaying and twisting to crosscutting interactions as the relative angle between extension directions increases during multiphase rifting. Our modeling results are consistent with observations of fault interaction styles in natural multiphase rifts, and the models provide theoretical examples that can be used to constrain the angle between extension directions in multiphase rifts from assessment of the fault interaction styles between first- and second-phase faults. A further implication of the observed variability in fault interaction styles is that our discrete element models are applicable for predicting fault patterns and the evolution of fault networks in multiphase rifts.

In general, reactivation of a preexisting fault depends on fault strength (e.g., Bellahsen & Daniel, 2005; Dubois et al., 2002; Etheridge, 1986; Ranalli & Yin, 1990), fault orientation (e.g., Bonini et al., 1997; Fazlikhani et al., 2017; Henza et al., 2010, 2011; Huyghe & Mugnier, 1992; Keep & McClay, 1997; Krantz, 1991; Phillips et al., 2016; Sibson, 1985), and the state of stress in three dimensions (e.g., Ranalli & Yin, 1990; Sibson, 1985). Although we focus on the control of the strike angle of a preexisting fault relative to the extension direction on its reactivation mode, the experiment setup of the preexisting fault, such as fault strength, length, and dip, is specifically chosen to avoid their effects on the modeling results. To achieve this, the preexisting fault in our models is defined to be weak enough and dipping favorably, and the models experience uniform extension, and hence, a change in these parameters may lead to different modeling results. Nevertheless, this work provides a theoretical example of studying the factors controlling the reactivation of a single preexisting fault and subsequent fault evolution.

5. Conclusion

Our numerical study of structural patterns forming during extension across a weak preexisting fault of variable strike orientation shows the following:

1. The strike angle (α) of a preexisting fault relative to the extension direction controls the reactivation mode. With a large α ($\geq$60°), a preexisting fault is fully reactivated. With an intermediate α (45°), a preexisting fault is partially reactivated. With a small α (30°), a preexisting fault is not reactivated.
2. A strain shadow zone (zone of reduced fault density) occurs around the plane of the fully reactivated fault with a large α ($\geq$60°). The size (length and width) of this zone is proportional to the length and displacement of the reactivated fault.
3. A preexisting fault that is fully reactivated obtains a large fault length early in its growth history. In comparison, a preexisting fault that is partly reactivated forms a few fault segments with small lengths and displacements.
4. A reactivated fault influences the orientation of adjacent new faults when the preexisting fault makes a high angle ($\alpha \geq 60°$) to the extension direction, generating new faults that are nearly perpendicular or highly oblique to the reactivated fault.
5. A fully reactivated fault enhances the displacements of fault segments linking to it, which masks their initial displacement maxima. Therefore, interpretation of the growth history of faults that link to and are affected by a fully reactivated fault based on the final displacement distribution or D-L plots is complicated.
6. Fault interaction styles depend on the reactivation pattern of the preexisting fault. There is a shift from splaying and twisting to crosscutting interactions with a decrease in the strike angle of the preexisting fault relative to the extension direction. The development of fault interaction styles can, to some extent, be used to constrain the angle between extension directions in multiphase rifts.

Acknowledgments
This contribution forms part of the MultiRift Project funded by the Research Council of Norway's PETROMAKS program (project 215591) and Statoil to the University of Bergen and partners Imperial College, University of Manchester and University of Oslo. We thank members of the MultiRift project for discussion, which helped focus the model presented in this paper. Schlumberger is thanked for academic Petrel licenses to the universities of Bergen and Manchester, which were used to visualize the numerical modeling results. Thanks to reviewer Giacomo Corti, David Sanderson, and editor John Geissman, Derek Keir, Debra Koch for constructive comments. The data can be obtained from the link folk.uib.no/nglhe/Publicationsdata.html.

References

Ackermann, R. V., & Schlische, R. W. (1997). Anticlustering of small normal faults around larger faults. *Geology*, *25*(12), 1127–1130.
Badley, M. E., Price, J. D., Dahl, C. R., & Agdestein, T. (1988). The structural evolution of the north Viking Graben and its bearing upon extensional modes of basin formation (North Sea). *Journal of the Geological Society*, *14*(3), 3686–3689.
Bardet, J. P., & Proubet, J. (1992). The structure of shear bands in idealized granular materials. *Applied Mechanics Reviews*, *45*(3), S118–S122.
Baudon, C., & Cartwright, J. A. (2008). 3D seismic characterisation of an array of blind normal faults in the levant basin, eastern Mediterranean. *Journal of Structural Geology*, *30*(6), 746–760.
Behn, M. D., Lin, J., & Zuber, M. T. (2002). A continuum mechanics model for normal faulting using a strain-rate softening rheology: Implications for thermal and rheological controls on continental and oceanic rifting. *Earth and Planetary Science Letters*, *202*(3), 725–740.
Bellahsen, N., & Daniel, J. M. (2005). Fault reactivation control on normal fault growth: An experimental study. *Journal of Structural Geology*, *27*(4), 769–780.
Bellahsen, N., Fournier, M., d'Acremont, E., Leroy, S., & Daniel, J. (2006). Fault reactivation and rift localization: Northeastern Gulf of Aden margin. *Tectonics*, *25*, TC1007. https://doi.org/10.1029/2004TC001626
Bonini, M., Souriot, T., Boccaletti, M., & Brun, J. P. (1997). Successive orthogonal and oblique extension episodes in a rift zone: Laboratory experiments with application to the Ethiopian rift. *Tectonics*, *16*(2), 347–362.
Cartwright, J., Trudgill, B. D., & Mansfield, C. S. (1995). Fault growth and segment linkage: An explanation for scatter in maximum displacement and trace length data from the Canyonlands grabens of Se Utah. *Journal of Structural Geology*, *17*(9), 1319–1326.
Childs, C., Watterson, J., & Walsh, J. J. (1995). Fault overlap zones within developing normal fault systems. *Journal of the Geological Society of London*, *152*(3), 535–549.
Claringbould, J. S., Bell, R. E., Jackson, A. L., Gawthorpe, R. L., & Odinsen, T. (2017). Pre-existing normal faults have limited control on the rift geometry of the northern North Sea. *Earth and Planetary Science Letters*, *475*, 190–206.
Contreras, J., Anders, M. H., & Scholz, C. H. (2000). Growth of a normal fault system: Observations from the Lake Malawi basin of the east African rift. *Journal of Structural Geology*, *22*(2), 159–168.
Corti, G. (2009). Continental rift evolution: From rift initiation to incipient break-up in the Main Ethiopian Rift, East Africa. *Earth Science Reviews*, *96*(1–2), 1–53.
Cowie, P., Gupta, S., & Dawers, N. (2000). Implications of fault array evolution for synrift depocentre development: Insights from a numerical fault growth model. *Basin Research*, *12*(3–4), 241–261.
Cowie, P. A., Underhill, J. R., Behn, M. D., Lin, J., & Gill, C. E. (2005). Spatio-temporal evolution of strain accumulation derived from multi-scale observations of Late Jurassic rifting in the northern North Sea: A critical test of models for lithospheric extension. *Earth and Planetary Science Letters*, *234*(3–4), 401–419.
Cundall, P. A. (1971). Distinct element models of rock and soil structure. In E. T. Brown (Ed.), *Analytical and computational methods in engineering rock mechanics* (pp. 129–163). London: Unwin Publishers.
Cundall, P. A., & Strack, O. (1979). A discrete numerical model for granular assemblies. *Géotechnique*, *29*(1), 47–65.
Davies, R., Turner, J., & Underhill, J. (2001). Sequential dip-slip fault movement during rifting: A new model for the evolution of the Jurassic trilete North Sea rift system. *Petroleum Geoscience*, *7*(4), 371–388.
Dawers, N. H., & Anders, M. H. (1995). Displacement-length scaling and fault linkage. *Journal of Structural Geology*, *17*(5), 607–614.
Deng, C., Fossen, H., Gawthorpe, R. L., Rotevatn, A., Jackson, A. L., & Fazlikhani, H. (2017). Influence of fault reactivation during multiphase rifting: The Oseberg area, northern North Sea rift. *Marine and Petroleum Geology*, *86*, 1252–1272.
Deng, C., Gawthorpe, R. L., Finch, E., & Fossen, H. (2017). Influence of a pre-existing basement weakness on normal fault growth during oblique extension: Insights from discrete element modeling. *Journal of Structural Geology*, *105*, 44–61.
Donzé, F., Mora, P., & Magnier, S.-A. (1994). Numerical simulation of faults and shear zones. *Geophysical Journal International*, *116*(1), 46–52.
Dubois, A., Odonne, F., Massonnat, G., Lebourg, T., & Fabre, R. (2002). Analogue modelling of fault reactivation: Tectonic inversion and oblique remobilisation of grabens. *Journal of Structural Geology*, *24*(11), 1741–1752.
Duffy, O. B., Bell, R. E., Jackson, C. A., Gawthorpe, R. L., & Whipp, P. S. (2015). Fault growth and interactions in a multiphase rift fault network: Horda Platform, Norwegian North Sea. *Journal of Structural Geology*, *80*, 99–119.
Egholm, D. L., Sandiford, M., Clausen, O. R., & Nielsen, S. B. (2007). A new strategy for discrete element numerical models: 2. Sandbox applications. *Journal of Geophysical Research*, *112*, B05204. https://doi.org/10.1029/2006JB004558
Enachescu, M. E. (1987). Tectonic and structural framework of the northeast Newfoundland continental margin. In C. Beaumont & A. J. Tankard (Eds.), *Sedimentary basins and basin-forming mechanisms* (Vol. 12, pp. 117–146). Calgary: Canadian Society of Petroleum Geologists Memoir.
Etheridge, M. A. (1986). On the reactivation of extensional fault systems. *Philosophical Transactions of the Royal Society of London. Series A, Mathematical and Physical Sciences*, *317*(1539), 179–194.
Færseth, R. (1996). Interaction of Permo-Triassic and Jurassic extensional fault-blocks during the development of the northern North Sea. *Journal of the Geological Society*, *153*(6), 931–944.
Færseth, R. B., Knudsen, B. E., Liljedahl, T., Midbøe, P. S., & Søderstrøm, B. (1997). Oblique rifting and sequential faulting in the Jurassic development of the northern North Sea. *Journal of Structural Geology*, *19*(10), 1285–1302.
Færseth, R. B., & Ravnås, R. (1998). Evolution of the oseberg fault-block in context of the northern North Sea structural framework. *Marine and Petroleum Geology*, *15*(5), 467–490.
Fazlikhani, H., Fossen, H., Gawthorpe, R. L., Faleide, J. I., & Bell, R. E. (2017). Basement structure and its influence on the structural configuration of the northern North Sea rift. *Tectonics*, *36*, 1151–1177. https://doi.org/10.1002/2017TC004514
Finch, E., & Gawthorpe, R. (2017). Growth and interaction of normal faults and fault network evolution in rifts: Insights from three-dimensional discrete element modelling. *Geological Society, London, Special Publications*, *439*.
Finch, E., Hardy, S., & Gawthorpe, R. (2003). Discrete element modelling of contractional fault-propagation folding above rigid basement fault blocks. *Journal of Structural Geology*, *25*(4), 515–528.
Finch, E., Hardy, S., & Gawthorpe, R. (2004). Discrete-element modelling of extensional fault-propagation folding above rigid basement fault blocks. *Basin Research*, *16*(4), 467–488.
Fossen, H., & Rotevatn, A. (2016). Fault linkage and relay structures in extensional settings—A review. *Earth-Science Reviews*, *154*, 14–28.
Frankowicz, E., & Mcclay, K. R. (2010). Extensional fault segmentation and linkages, Bonaparte Basin, outer North West shelf, Australia. *AAPG Bulletin*, *94*(7), 977–1010.
Gawthorpe, R., & Leeder, M. (2000). Tectono-sedimentary evolution of active extensional basins. *Basin Research*, *12*(3–4), 195–218.

Gawthorpe, R. L., Jackson, C. A.-L., Young, M. J., Sharp, I. R., Moustafa, A. R., & Leppard, C. W. (2003). Normal fault growth, displacement localisation and the evolution of normal fault populations: The Hammam Faraun fault block, Suez rift, Egypt. *Journal of Structural Geology*, *25*, 883–895.

Giba, M., Walsh, J. J., & Nicol, A. (2012). Segmentation and growth of an obliquely reactivated normal fault. *Journal of Structural Geology*, *39*, 253–267.

Hardy, S. (2013). Propagation of blind normal faults to the surface in basaltic sequences: Insights from 2D discrete element modelling. *Marine and Petroleum Geology*, *48*(2), 149–159.

Hardy, S., & Finch, E. (2005). Discrete-element modelling of detachment folding. *Basin Research*, *17*(4), 507–520.

Hardy, S., & Finch, E. (2006). Discrete element modelling of the influence of cover strength on basement-involved fault-propagation folding. *Tectonophysics*, *415*(1), 225–238.

Hardy, S., & Finch, E. (2007). Mechanical stratigraphy and the transition from trishear to kink-band fault-propagation fold forms above blind basement thrust faults: A discrete-element study. *Marine and Petroleum Geology*, *24*(2), 75–90.

Henza, A. A., Withjack, M. O., & Schlische, R. W. (2010). Normal-fault development during two phases of non-coaxial extension: An experimental study. *Journal of Structural Geology*, *32*(11), 1656–1667.

Henza, A. A., Withjack, M. O., & Schlische, R. W. (2011). How do the properties of a pre-existing normal-fault population influence fault development during a subsequent phase of extension? *Journal of Structural Geology*, *33*(9), 1312–1324.

Homberg, C., Angelier, J., Bergerat, F., & Lacombe, O. (2004). Erratum to "using stress deflections to identify slip events in fault systems": [earth planet. sci. lett. 217 (2004) 409–424]. *Earth and Planetary Science Letters*, *220*(3–4), 453–454.

Homberg, C., Hu, J. C., Angelier, J., Bergerat, F., & Lacombe, O. (1997). Characterization of stress perturbations near major fault zones: Insights from 2D distinct-element numerical modelling and field studies (Jura mountains). *Journal of Structural Geology*, *19*(5), 703–718.

Huggins, P., Watterson, J., Walsh, J. J., & Childs, C. (1995). Relay zone geometry and displacement transfer between normal faults recorded in coal-mine plans. *Journal of Structural Geology*, *17*(12), 1741–1755.

Huismans, R. S., & Beaumont, C. (2007). Roles of lithospheric strain softening and heterogeneity in determining the geometry of rifts and continental margins. In G. D. Karner, G. Manatschal, & L. M. Pinheiro (Eds.), *Imaging, mapping and modelling continental lithosphere extension and breakup* (Vol. 282, pp. 111–138). London: Geological Society, London, Special Publications.

Huyghe, P., & Mugnier, J. L. (1992). The influence of depth on reactivation in normal faulting. *Journal of Structural Geology*, *14*(8–9), 991–998.

Imber, J., Tuckwell, G. W., Childs, C., Walsh, J. J., Manzocchi, T., Heath, A. E., et al. (2004). Three-dimensional distinct element modelling of relay growth and breaching along normal faults. *Journal of Structural Geology*, *26*(10), 1897–1911.

Jackson, C. A.-L., Gawthorpe, R. L., & Sharp, I. R. (2002). Growth and linkage of the East Tanka Fault Zone: Structural style and syn-rift stratigraphic response. *Geological Society of London*, *159*(2), 175–187.

Jackson, C. A.-L., & Rotevatn, A. (2013). 3D seismic analysis of the structure and evolution of a salt-influenced normal fault zone: A test of competing fault growth models. *Journal of Structural Geology*, *54*, 215–234.

Keep, M., & McClay, K. (1997). Analogue modelling of multiphase rift systems. *Tectonophysics*, *273*(3–4), 239–270.

King, G. C. P., Stein, R. S., & Rundle, J. B. (1988). The growth of geological structures by repeated earthquakes 1. Conceptual framework. *Journal of Geophysical Research*, *93*(B11), 13,307–13,318.

Komoróczi, A., Abe, S., & Ueai, J. L. (2013). Meshless numerical modelling of brittle-viscous deformation: First results on boudinage and hydrofracturing using a coupling of discrete element method (DEM) and smoothed particle hydrodynamics (SPH). *Computers and Geosciences*, *17*, 373–390.

Krantz, R. W. (1991). Normal fault geometry and fault reactivation in tectonic inversion experiments. *Geological Society of London, Special Publication*, *56*(1), 219–229.

Kuhn, M. R. (1999). Structured deformation in granular materials. *Mechanics of Materials*, *31*(6), 407–429.

Kusznir, N. J., & Park, R. G. (1987). The extensional strength of the continental lithosphere: Its dependence on geothermal gradient, and crustal composition and thickness. *Geological Society, London, Special Publications*, *28*(1), 35–52.

Le Turdu, C., Tiercelin, J.-J., Richert, J.-P., Rolet, J., Xavier, X.-P., Renaut, R. W., et al. (1999). Influence of pre-existing oblique discontinuities on the geometry and evolution of extensional fault patterns: Evidence from the Kenya rift using SPOT imagery. In C. K. Morley (Ed.), *Geoscience of rift systems—Evolution of East Africa* (Vol. 44, pp. 173–191). Tulsa, OK: American Association of Petroleum Geologists Studies in Geology.

Lepvrier, C., Fournier, M., Bérard, T., & Roger, J. (2002). Cenozoic extension in coastal Dhofar (southern Oman): Implications on the oblique rifting of the Gulf of Aden. *Tectonophysics*, *357*(1–4), 279–293.

Lezzar, K. E., Tiercelin, J. J., Turdu, C. L., Cohen, A. S., Reynolds, D. J., Gall, B. L., et al. (2002). Control of normal fault interaction of major Neogene sedimentary depocenters, Lake Tanganyika, East African rift. *AAPG Bulletin*, *86*(6), 1027–1059.

Mansfield, C. S., & Cartwright, J. A. (1995). Fault growth by linkage: Observations and implications from analogue models. *Journal of Structural Geology*, *23*(5), 745–763.

McLeod, A., Dawers, N. H., & Underhill, J. R. (2000). The propagation and linkage of normal faults: Insights from the Strathspey-Brent-Statfjord fault array, northern North Sea. *Basin Research*, *12*(3–4), 263–284.

Meyer, V., Nicol, A., Childs, C., Walsh, J., & Watterson, J. (2002). Progressive localisation of strain during the evolution of a normal fault population. *Journal of Structural Geology*, *24*(8), 1215–1231.

Mora, P., & Place, D. (1993). A lattice solid model for the non-linear dynamics of earthquakes. *International Journal of Modern Physics C*, *4*(6), 1059–1074.

Mora, P., & Place, D. (1994). Simulation of the frictional stick-slip instability. *Pure and Applied Geophysics*, *143*(1–3), 61–87.

Mora, P., & Place, D. (1998). Numerical simulation of earthquake faults with gouge: Toward a comprehensive explanation for the heat flow paradox. *Journal of Geophysical Research*, *103*(B9), 21,067–21,089.

Morley, C., Gabdi, S., & Seusutthiya, K. (2007). Fault superimposition and linkage resulting from stress changes during rifting: Examples from 3D seismic data, Phitsanulok Basin, Thailand. *Journal of Structural Geology*, *29*(4), 646–663.

Morley, C., Haranya, C., Phoosongsee, W., Pongwapee, S., Kornsawan, A., & Wonganan, N. (2004). Activation of rift oblique and rift parallel pre-existing fabrics during extension and their effect on deformation style: Examples from the rifts of Thailand. *Journal of Structural Geology*, *26*(10), 1803–1829.

Morley, C. K. (1999). Patterns of displacement along large normal faults; Implications for basin evolution and fault propagation, based on examples from East Africa. *AAPG Bulletin*, *83*(4), 613–634.

Morley, C. K., Nelson, R. A., Patton, T. L., & Munn, S. G. (1990). Transfer zones in the East African rift system and their relevance to hydrocarbon exploration in rifts. *AAPG Bulletin*, *74*(8), 1234–1253.

Muirhead, J. D., & Kattenhorn, S. A. (2017). Activation of preexisting transverse structures in an evolving magmatic rift in East Africa. *Journal of Structural Geology*, *106*, 1–18.

Nicol, A., Walsh, J. J., Watterson, J., & Underhill, J. R. (1997). Displacement rates of normal faults. *Nature*, *390*(6656), 157–159.
Nixon, C. W., Sanderson, D. J., Dee, S. J., Bull, J. M., Humphreys, R. J., & Swanson, M. H. (2014). Fault interactions and reactivation within a normal-fault network at Milne Point, Alaska. *AAPG Bulletin*, *98*(10), 2081–2107.
Odinsen, T., Reemst, P., Beek, P. V. D., Faleide, J. I., & Gabrielsen, R. H. (2000). Permo-Triassic and Jurassic extension in the northern North Sea: Results from tectonostratigraphic forward modelling. *Geological Society, London, Special Publications*, *167*, 83–103.
Phillips, T. B., Jackson, A. L., Bell, R. E., Duffy, O. B., & Fossen, H. (2016). Reactivation of intrabasement structures during rifting: A case study from offshore southern Norway. *Journal of Structural Geology*, *91*, 54–73.
Place, D. G., & Mora, P. R. (2001). A random lattice solid model for simulation of fault zone dynamics and fracture processes. In H. B. Mulhaus, A. V. Dyskin, & E. Pasternak (Eds.), *Bifurcation and Localisation Theory for Soils and Rocks '99* (pp. 321–333). Rotterdam, Netherlands: A.A. Balkema.
Ranalli, G. (1995). *Rheology of the Earth* (2nd ed.). London: Chapman and Hall.
Ranalli, G., & Yin, Z. M. (1990). Critical stress difference and orientation of faults in rocks with strength anisotropies: The two-dimensional case. *Journal of Structural Geology*, *12*(8), 1067–1071.
Rykkelid, E., & Fossen, H. (2002). Layer rotation around vertical fault overlap zones: Observations from seismic data, field examples, and physical experiments. *Marine and Petroleum Geology*, *19*(2), 181–192.
Schlische, R. W., & Anders, M. H. (1996). Stratigraphic effects and tectonic implications of the growth of normal faults and extensional basins. In K. K. Beratan (Eds), *Reconstructing the History of Basin and Range Extension Using Sedimentology and Stratigraphy* (Vol. 303, pp. 183–203). Boulder, CO: Geological Society of America Special Publication.
Schöpfer, M. P. J., Childs, C., & Walsh, J. J. (2006). Localisation of normal faults in multilayer sequences. *Journal of Structural Geology*, *28*(5), 816–833.
Schöpfer, M. P. J., Childs, C., & Walsh, J. J. (2007a). Two-dimensional distinct element modeling of the structure and growth of normal faults in multilayer sequences: 1. Model calibration, boundary conditions, and selected results. *Journal of Geophysical Research*, *112*, B10401. https://doi.org/10.1029/2006JB004902
Schöpfer, M. P. J., Childs, C., & Walsh, J. J. (2007b). 2D distinct element modeling of the structure and growth of normal faults in multilayer sequences: 2. Impact of confining pressure and strength contrast on fault zone growth and geometry. *Journal of Geophysical Research*, *112*, B10401. https://doi.org/10.1029/2006JB004902
Sibson, R. H. (1985). A note on fault reactivation. *Journal of Structural Geology*, *7*(6), 751–754.
Sinclair, I. K. (1995a). Transpressional inversion due to episodic rotation of extensional stresses in Jeanne d'Arc Basin, offshore Newfoundland. In J. G. Buchanan & P. G. Buchanan (Eds.), *Basin inversion* (Vol. 88, pp. 249–271). Geological Society, London, Special Publication.
Sinclair, I. K. (1995b). Sequence stratigraphic response to Aptian–Albian rifting in conjugate margin basins: A comparison of the Jeanne d'Arc Basin, offshore Newfoundland, and the Porcupine Basin, offshore Ireland. In R. A. Scrutton, M. S. Stoker, G. B. Shimmield, & A. W. Tudhope (Eds.), *The tectonics, sedimentation, and palaeoceanography of the North Atlantic region* (Vol. 90, pp. 29–49). Geological Society, London, Special Publication.
Tomasso, M., Underhill, J. R., Hodgkinson, R. A., & Young, M. J. (2008). Structural styles and depositional architecture in the triassic of the ninian and alwyn north fields: implications for basin development and prospectivity in the northern north sea. *Marine & Petroleum Geology*, *25*(7), 588–605.
Trudgill, B., & Cartwright, J. A. (1994). Relay-ramp forms and normal fault linkages, Canyonlands National Park, Utah. *Geological Society of America Bulletin*, *106*(9), 1143–1157.
Walsh, J., Nicol, A., & Childs, C. (2002). An alternative model for the growth of faults. *Journal of Structural Geology*, *24*(11), 1669–1675.
Walsh, J. J., Bailey, W. R., Childs, C., Nicol, A., & Bonson, C. G. (2003). Formation of segmented normal faults: A 3-D perspective. *Journal of Structural Geology*, *25*(8), 1251–1262.
Walsh, J. J., & Watterson, J. (1988). Analysis of the relationship between displacements and dimensions of faults. *Journal of Structural Geology*, *10*(3), 239–247.
Wenk, L., & Huhn, K. (2013). The influence of an embedded viscoelastic–plastic layer on kinematics and mass transport pattern within accretionary wedges. *Tectonophysics*, *608*(47), 653–666.
Whipp, P., Jackson, C., Gawthorpe, R., Dreyer, T., & Quinn, D. (2014). Normal fault array evolution above a reactivated rift fabric; A subsurface example from the northern Horda Platform, Norwegian North Sea. *Basin Research*, *26*(4), 523–549.
Young, M. J., Gawthorpe, R. L., & Hardy, S. (2001). Growth and linkage of a segmented normal fault zone; The Late Jurassic Murchison-Statfjord North Fault, northern North Sea. *Journal of Structural Geology*, *23*(12), 1933–1952.